OUTER SPHERE REDOX CHEMISTRY FOR RECHARGEABLE FLOW BATTERIES

A Thesis submitted to
Indian **I**nstitute of **S**cience **E**ducation and **R**esearch (**IISER**), **P**une
in partial fulfilment of the requirements for the
BS-MS Dual Degree Programme

by

ABDUL RAAFIK. A. T
(Registration No: 20151027)

Indian **I**nstitute of **S**cience **E**ducation and **R**esearch (**IISER**), **P**une
Dr. Homi Bhabha Road,
Pashan, Pune-411008, INDIA.

April, **2020**

Supervisor:
Dr. MUHAMMED MUSTHAFA O T
(Associate Professor, Department of Chemistry, IISER, Pune)

CERTIFICATE

This is to certify that this dissertation entitled **"Outer Sphere Redox Chemistry for Rechargeable Flow Batteries"** towards the partial fulfilment of the BS-MS dual degree programme at the Indian Institute of Science Education and Research, Pune represents study/work carried out by **Abdul Raafik. A. T (Reg. No: 20151027)** at Indian Institute of Science Education and Research (IISER), Pune under the supervision of **Dr. Muhammed Musthafa. O. T, Associate Professor, Department of Chemistry, IISER Pune** during the academic year 2019-2020.

Date: **29/ 03/ 2020**
Place: **Pune**

Dr. Muhammed Musthafa. O. T
Associate Professor
Department of Chemistry
Indian **I**nstitute of **S**cience **E**ducation and **R**esearch
Pune-411008, India.

Abdul Raafik. A. T
(Reg. No: 20151027)

DECLARATION

I hereby declare that the research work presented in the report entitled **"Outer Sphere Redox Chemistry for Rechargeable Flow Batteries"** have been carried out by me at the **Department of Chemistry, Indian Institute of Science Education and Research, Pune** under the supervision of **Dr. Muhammed Musthafa. O. T** and the same has not been submitted elsewhere for any degree.

Date: **29/ 03/ 2020**
Place: **Pune**

Abdul Raafik. A. T
(Registration No: 20151027)

Dr. Muhammed Musthafa. O. T
Associate Professor
Department of Chemistry
Indian **I**nstitute of **S**cience **E**ducation and **R**esearch
Pune-411008, India.

ACKNOWLEDGEMENTS

This venture wouldn't have been possible without the continuous involvement of my family, teachers, and friends. I cannot thank enough for the infinite amount of care, love, and support from my parents throughout my whole life. I would like to express my immense gratitude to my supervisor **Dr. Musthafa** for his guidance and motivation throughout my electrochemistry research career. I always indebted to him for his invaluable mentorship resulted in the successful completion of my project. Along with Dr. Musthafa, I thank my additional TAC expert member **Prof. P. A. Joy** (Chair, Physical and Materials Chemistry Division, CSIR- National Chemical Laboratory, Pune), for his valuable suggestions during my presentations and report submissions. Their useful inputs helped me to improve my result, inference, etc. presentation skills to address the questions in a pinpoint manner within the scope of my work. All my colleagues were equally crucial for the gradual development of my experimental, analytical as well as result presentation skills which were essential during my project. I thank Pramod Gaikwad for initially introducing me to various electrochemical applications and teaching me basic electrochemical characterization techniques. I thank Manu Gautam and Dr. Mruthyunjayachari (Madhu sir) for teaching & assisting me with various material syntheses, battery fabrication, as well as material characterizations works. I thank Alagar Raja and Neethu.C. D for teaching me advanced electrochemical characterization techniques along with their constant valuable lessons on fundamental aspects of electrochemistry. I appreciate all other lab members, especially Zahid Bhat & Madhu sir, for continuous mentoring by teaching me various analytical skills, invaluable advice when I get stuck, clearing my doubts, correcting when I get wrong, and along with all, the priceless fun moments throughout my career at Dr. Musthafa's group. I would like to thank my batchmates and seniors; Neethu C D, Muhammed Fawaz, Shana Shirin, Kausal A K, Aysha Basheer, Akber Hussain, Muhammed Rizal, Haritha A S for regularly assisting me in difficult times in coursework as well as my college life. I thank IISER Pune for all the laboratory facilities to carry out my research works. I acknowledge DST- INPIRE for their financial support. I especially acknowledge Dr. Vinod (National Chemical Laboratory) for the XPS facility and Savitribai Phule Pune University for ATR-FTIR facility for my project purpose.

CONTENT

LIST OF FIGURES

LIST OF TABLES

ABSTRACT

Reversible redox species play central role as electron acceptors in state-of-the-art flow batteries and fuel cells. At electrochemical interfaces, since the physical processes of mass transport occurs independently and in series to electron transport; the reaction velocity in reversible species is predominantly transport controlled due to their fast electron transfer events. Thus, the physical processes of bringing the reactants together play central roles in the electrochemistry of reversible redox molecules (because their extremely fast electron transfer events demand the reacting species to reach the reaction zone by simple diffusion). Even under convective fluid flow, spatial structuring of the solution forces simple diffusion to dominate the transport phenomena near the electrode, which in turn poses unique challenges to utilize the full potential of the molecules either by the electrode or fluid characteristics. This translates into extremely low volumetric energy density in flow batteries, and in the attempts to target it are mainly carried out by improving the solubility limits, whereas the root of the problem being their transport-controlled reaction velocity is often overlooked. We show that Coulombic force gated molecular flux almost doubles the volumetric energy density in reversible species-based flow batteries by generating an electrostatic current parallel to the diffusion current.

CHAPTER 1

INTRODUCTION

Population explosion and rapid industrialization have intensely increased our energy demands.[1] Traditional non-renewable hydrocarbon combustion engines have brought immense pollution and global warming due to its harmful green-house gas emissions.[1-3] To cope up with our growing energy demands sustainably, we need to shift our focus from non-renewable resources to renewable alternatives.[2,3] However, there are several geographical as well as time availability constraints for such resources. Electrochemical systems such as batteries, fuel cells, electrochemical capacitors are a better option to store and convert such energy according to our needs.[2-14] The key processes occurring in the electrode-electrolyte interface plays a significant role in the energy as well as power density drawn out of the electrochemical energy conversion system.

Various electrochemical energy & conversion devices show different behaviour in terms of energy and power. The Ragone plot is a clear representation (figure 1.1a), which shows the high energy characteristic of the fuel cells, the high-power characteristic of supercapacitors, and the intermediate nature of the batteries. Compared to fuel cells and supercapacitors, batteries have an established position in the market make it more accessible and popular.[6-17]

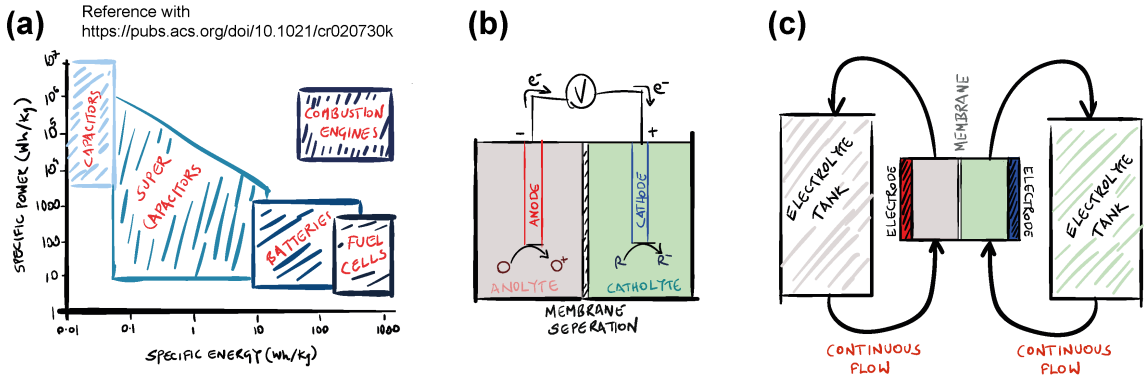

Figure 1.1: (a) A simplified schematic representation of Ragone plot. **(b)** A voltaic cell schematic representation. **(c)** A redox flow cell simplified representation.

1.1. Batteries:

Batteries are the type of electrochemical storage, and conversion devices consist atleast one voltaic cell which stores chemical energy and converts to electric power as per requirement. A voltaic cell consists of two half cells, i.e., a heterogeneous oxidation and reduction reactions happening on the anode and cathode electrode-electrolyte interface, respectively, which is separated by a semi-permeable membrane and connected to an external circuit (which primarily uses up the stored chemical energy) (figure 1.1b).[6-17]

1.1.1. Primary and Secondary Batteries:

In a primary battery system, as the electricity is getting consumed, the oxidizing (anolyte) and the reducing material (catholyte) will be undergoing an electrically irreversible chemical reaction.[6,7] Primary batteries are constructed in such a way to be discarded when the current drops to zero due to the complete consumption of anolyte/catholyte. Whereas in the case of secondary batteries, the anolyte/catholyte will be electrochemically reversible, which could be electrically charged externally.[8-17]

1.1.2. Redox Flow Batteries:

Flow batteries or redox flow batteries are known for their commercial success due to its cheap maintenance and tunability.[10-17] Although the chemistry seems similar, these flow batteries have very good advantages over the stagnant type flooded-batteries. A flow cell has a mechanism, as shown in the figure 1.1c where the anolyte-catholyte redox species are pumped continuously into the cell separated by a membrane. Here the battery capacity could be increased easily by just changing the tank size without effecting the power simultaneously because power rating depends on the active area where reaction happens. So, the lifetime of the battery could be increased, just increasing the tank capacity. This convenience interestingly reduces the maintenance cost also.[12-17]

1.2. Electron Transfer Mechanisms:

As mentioned in the first paragraph of the chapter, in an electrochemical system, the electron transfer reaction (oxidation or reduction) happens at the electrode-electrolyte interface. This reaction could happen either through the inner-sphere or the outer-sphere mechanistic pathway, depending upon the redox-active species at the interface.[19-26]

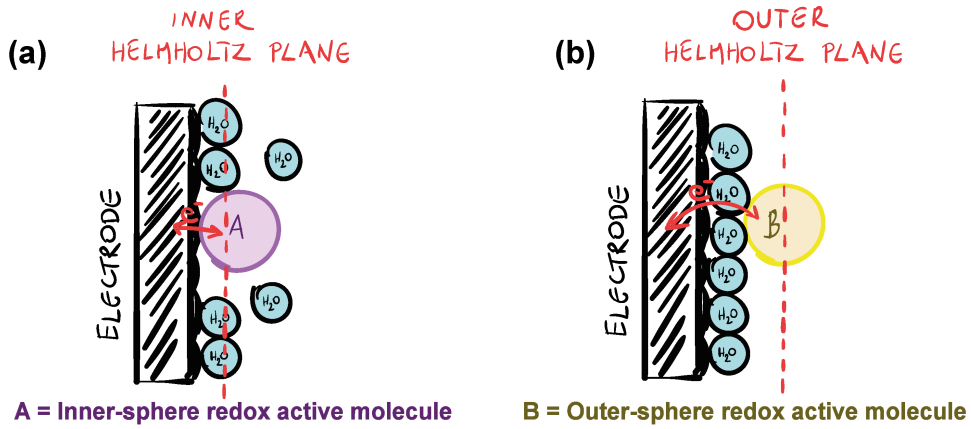

Figure 1.2: Schematic representation: **(a)** Inner-sphere electron transfer. **(b)** Outer-sphere electron transfer representation.

1.2.1. Inner-Sphere Characteristics:

In electrochemistry, an inner-sphere mechanistic pathway means the active redox molecule makes an actual bond with the electrode for the electron transfer purpose (figure 1.2a). So, it is evident that the species should be at the inner Helmholtz plane overcoming the solvated molecules barrier in an electrolyte. Furthermore, this bond making process makes the electrode a prime component determining the rate of electroactive species conversion along with the catalytic activity of the electrode. The characteristics of such reactions depends upon the electrocatalysts used. Oxygen reduction reaction and Methanol oxidation reactions are the examples of inner sphere electron transfer.[19-26]

1.2.2. Outer-Sphere Characteristics:

In case of outer sphere electron transfer, active species does not make an actual bond with the electrode makes the electron transfer takes place through tunnelling (figure 1.2b). The electron transfer reaction is actively happening at the outer Helmholtz plane, ultimately suggests that the solvation is intact and the

electroactive species does not have to overcome the solvation barrier. Moreover, there is no bond formation, means it does not have any effect on the electrode's catalytic properties.[19-26]

These outer-sphere/inner-sphere pathways have a very significant impact on the rate as well as the energy requirement to carry out a particular electron transfer reaction. An outer-sphere electron transfer will occur at a much faster rate because there are no time-consuming processes, such as bond formation/dissociation & overcoming the solvation barrier involved here. Since these processes are absent, the electroactive species will not be needing to spend much energy to carry out the reaction.

1.3. Modes of Mass Transfer:

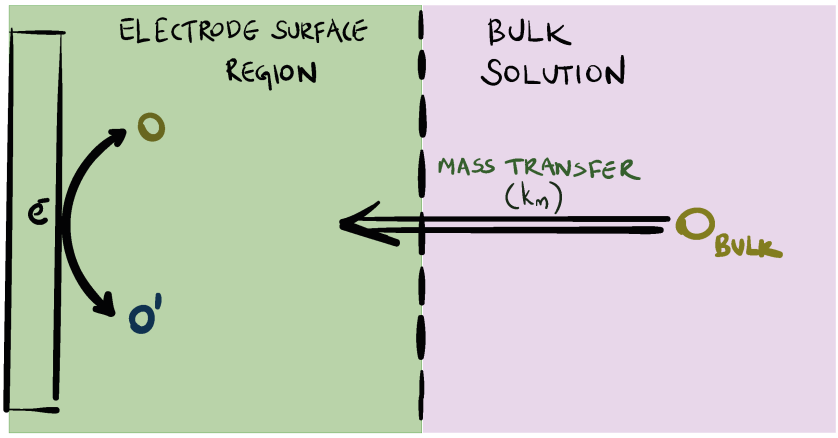

Figure 1.3: Mass transfer from bulk to electrode surface rate- A schematic representation (O=concentration of electroactive species at the surface, O'= concentration of converted product, O_{BULK}= concentration of O in the bulk, k_m= mass transfer coefficient).

Since the electrochemical conversion reaction is happening at the electrode-electrolyte interface, the concentration of electroactive species at the interface is the central component which determine the reaction rate and thereby the current generated. In an electrochemical system, this 'mass transfer' from bulk to the interface is controlled by three significant processes i.e., diffusion, migration, and convection (figure 1.3). The mass flux due to these processes are modelled with the help of Nernst-Plank equation (equation 1).[29-33]

$$J_i(x) = -\overbrace{D_i \frac{\partial C_i(x)}{\partial x}}^{\text{diffusion term}} - \overbrace{\frac{z_i F}{RT} D_i C_i \frac{\partial \phi(x)}{\partial x}}^{\text{migration term}} + \overbrace{C_i \upsilon(x)}^{\text{convection term}} \qquad \textbf{(Equation 1)}$$

($J_i(x)$= flux of species i at distance x from surface (mol cm^{-2} s^{-1}), D_i= diffusion coefficient (cm^2 s^{-1}), $\frac{\partial C_i(x)}{\partial x}$= concentration of i at distance x (mol cm^{-4}), $\frac{\partial \phi(x)}{\partial x}$= potential gradient (V cm^{-1}), z_i= number of charge, C_i= concentration of species i (mol cm^{-3}), $\upsilon(x)$= velocity (cm s^{-1}), R= gas constant (J mol^{-1} K^{-1}), F= Faraday constant (F), T= temperature (K))

1.3.1. *Diffusion:*

Mass transport controlled by diffusion is purely due to the concentration gradient within the solution, particularly between the interface and bulk region. The reaction happening at the electrode will cause a decrease in the concerned species and cause a flux from bulk to interface; similarly, the converted product will have a flux from the interface to bulk region due to its concentration gradient.[29-33]

1.3.2. *Migration:*

This mass transfer process is caused on the electroactive species, purely because of its ionic charge and the creation of local electrostatic fields which facilitates the movement. This transfer process due to the developed potential gradient is termed as migration. This effect is often nullified for the ease of studying an electrochemical system by adding a higher amount of supporting electrolyte compared to electroactive species concentration.[29-33]

1.3.3. *Convection:*

Convection term is explained as the hydrodynamic transport where the movement is caused by a forced disturbance in the solution such as stirring, rotating electrode & laminar flow (forced convection) along with the density gradient experienced within the solution (natural convection).[26-30]

Rotating Disk Electrode (RDE) and Rotating Ring Disk Electrode (RRDE) are two hydrodynamic technique which facilitates forced convection, making the system just diffusion-controlled and simplifies the system for fundamental studies.[17]

In state-of-the-art energy conversion and storage devices, the cathode often limits the overall performance metrics.[4-14] Negatively charged reversible species such as ferricyanide has been employed as the positive electrode in all alkaline quinone flow batteries, iron flow batteries, direct alcohol fuel cells, etc.[15-25] Since ferricyanide is a reversible redox species, its electrochemical behaviour is predominantly diffusion-controlled, which in turn poses unique challenges to target its overall reaction velocity purely by electrode characteristics.[26-29] It should be noted that even under convective fluid flow, the major mode of mass transport within the reaction zone is by simple diffusion due to an order large thickness of the hydrodynamic boundary layer compared to the diffusion layer.[30,31]

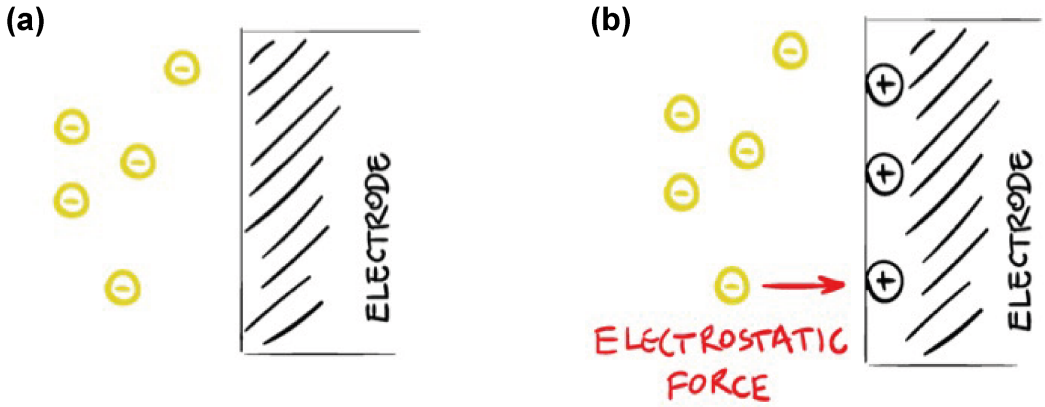

Figure 1.4: Schematic representation of introducing surface charge at electrode to invoke electrostatic force for mass transfer increment: **(a)** absence of incorporated surface charge, **(b)** presence of incorporated surface charge.

In electrochemical energy devices, these prevent the utilization of the full potential of reversible species either by the electrode or fluid characteristics, which in turn is responsible for their extremely low volumetric energy density (~20% of its theoretical value).[16,23] Although efforts are dedicated to overcoming these hurdles primarily by increasing the solubility of the redox species[21,32] and recently by chemical regeneration of the active species in external tanks[33], the root of the problem being their transport-controlled reaction velocity is often overlooked. Here, we show that by

activating Coulombic forces at the interface, gated molecular transport can be achieved to target the transport velocity of reversible species within the reaction zone. We demonstrate that this Coulombic force gated molecular flux can trigger an electrostatic current contribution parallel to the diffusion current within the reaction zone. By incorporating Coulombic forces (figure 1.4) in an iron-based redox flow battery, we show that gated molecular flux almost doubles the volumetric energy density without compromising the power capability by extending the concentration polarization regime beyond conventionally accessible limits.

As explained above, the mass transfer has a very significant effect in controlling the reaction rate, especially in an outer-sphere mechanism mediated electron transfer reactions. In such reactions with fast electron transfer kinetics, the mass transfer process will become a crucial limiting step essentially making the rate of reaction equal to the rate of mass transfer (equation 2).[55,56]

$$\boldsymbol{\upsilon_{rxn} = \upsilon_{mt} = \frac{i}{nFA}} \qquad \textbf{(Equation 2)}$$

(υ_{rxn}= rate of reaction (cm s^{-1}), υ_{mt} = rate of mass transfer (cm s^{-1}), i= current (A), n= number of charge, F= Faraday constant (~96500 C), A= area of the electrode (cm^2))

Within the context of the thesis, a thorough analysis was carried out on two iron-based species viz. ferri/ferrocyanide couple and iron(II/III)triethanolamine complex. Both of these redox couples are known to undergo outer sphere redox electron transfer and hence the performance is dependent on the mass transfer rather than kinetics at electrode. The studies mainly focused on modifying the polarity of electrodes, thereby tuning the mass transfer coefficient to obtain a higher mass transfer rate, which will cause a higher reaction rate in these outer-sphere redox species. The whole idea will increase the scope of redox flow batteries where the battery capacity could be enhanced without risking the power rating as well as the amount of electrolyte (tank capacity), as mentioned in section 1.1.2. Moreover, an all iron-based battery with modified electrodes demonstrated high performance compared to the unmodified ones.

CHAPTER 2

MATERIALS & METHODS

This chapter discusses the various experimental methods, electrochemical as well as material characterization techniques & analyses used throughout the project.

2.1. Chemicals:

Potassium ferricyanide, Potassium ferrocyanide, Iron(III) chloride (anhydrous), Iron(II) chloride (tetrahydrate), Triethanolamine, Potassium Hydroxide, Carbon nanotubes (multi-walled), Hydrochloric acid (36%), Poly(diallyldimethylammonium chloride) solution (20 wt. %), Nafion® perfluorinated resin solution (5 wt. %), Isopropyl alcohol.

2.2. Material Synthesis:

2.2.1. Multi-walled Carbon Nanotubes (CNT) Modification:

The pristine-CNT obtained commercially is further purified with the standard procedure by refluxing in 6M HCl at 60°C for 24 hours.[44-47] After this period, the dispersed solution is subjected to vacuum filtration along with multiple hot water wash and ethanol wash. The obtained CNT sampled are dried in a hot air oven (60°C) and afterward crushed into fine powder form. The pre-treated samples are then used for further analysis and to synthesize modified CNT forms.

For the positively charged carbon nanotube (P-CNT) synthesis, 0.1g of purified CNT is dispersed in a 1.5% (v/v) Poly(diallyldimethylammonium chloride) (PDDA) in 100 ml of distilled water by sonicating it for 2 hours.[40-43] In the negatively charge (N-CNT) case, the purified CNT is dispersed in a 2% (v/v) Nafion® solution in 100mL of distilled water followed by sonication for 2 hours.[45,46] The workup procedure has been carried out similarly to the pristine CNT case, as explained above. The modified CNTs are expected to be having non-covalent interactions with respective polymers as depicted in the figure 2.1 following previous studies.[40-46]

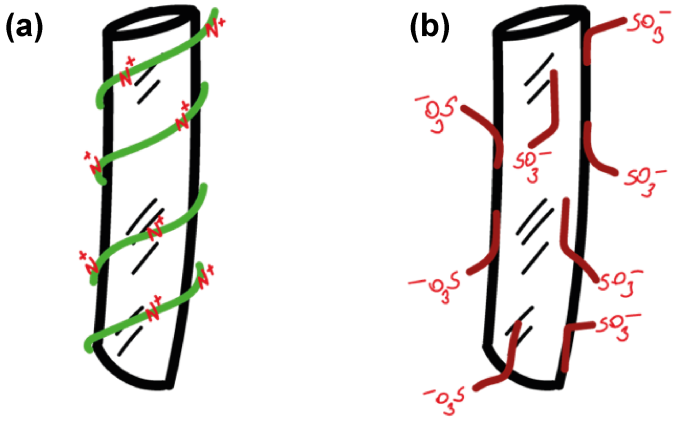

Figure 2.1: Schematic representation of CNT modification to form **(a)** P-CNT and **(b)** N-CNT by respective PDDA and Nafion® polymers.

2.2.2. *Redox-active Molecule Preparation:*

The electrochemical behaviours are studied on two redox-active systems i.e. $[Fe(CN)_6]^{4-}$/ $[Fe(CN)_6]^{3-}$ and $Fe[(TEOA)OH]^{-}$ / $Fe[(TEOA)(OH)]^{2-}$. Commercially available potassium ferricyanide or potassium ferrocyanide molecule is used to obtain the $[Fe(CN)_6]^{4-}$/ $[Fe(CN)_6]^{3-}$ redox-species system. The $Fe[(TEOA)OH]^{-}$ and $Fe[(TEOA)OH]^{2-}$ complexes are obtained by mixing $FeCl_2$ and $FeCl_3$, respectively, with triethanolamine in a 1:5 ratio under pH 13 alkaline KOH condition.[14]

2.3. Experimental Section:

2.3.1. *Electrochemical Characterization:*

All the electrochemical characterization experiments were carried out in accordance with below explained techniques. The chemicals and electrode used for each analysis is given along with the respective response figures. Drop-casted glassy carbon WE were used to conduct studies on materials i.e., CNT, P-CNT, and N-CNT. The drop cast ink is obtained by dispersing the powder samples in the minimum amount of IPA.

The cyclic voltammetry, chronoamperometry, and impedance spectroscopy studies were carried out in 3 electrode setup. And the linear scan voltammetry studies are carried in a rotating disk electrode (hydrodynamic technique) way in different RPMs. The instruments used for different experiments are shown in table 2.2.

The experiments were carried out in a three-electrode configuration where the current is measured between the working electrode (WE) & the counter electrode (CE) whereas the potential is determined with respect to a reference electrode (RE). Different WEs used during experiments are shown in the table 2.1 (specific details are explained with each experimental result). Throughout the experiments, all WEs are cleaned according to the standard manual polishing as well as electrochemical cleaning methods. A Hg/HgO (1M NaOH) RE and a platinum (Pt) disk CE was used in the configuration in all experiments.

Table 2.1: Electrodes and respective dimensions used within the experiments.

Electrode	Diameter (mm)
Glassy Carbon (GC)	3 mm
RDE GC	5 mm
Platinum (Pt)	2 mm
Gold (Au)	2 mm

Cyclic Voltammetry:

Cyclic Voltammetry (CV) is the most common electrochemical characterization technique used to study the electron transfer involved during electrochemical oxidation and reduction reactions. A Cyclic Voltammetry profile consists of applied potential, and current axes which sweeps from an initial potential (say) E_1 and a switching potential E_2 further the potential get swept back to E_1(figure 2.2a).[34]

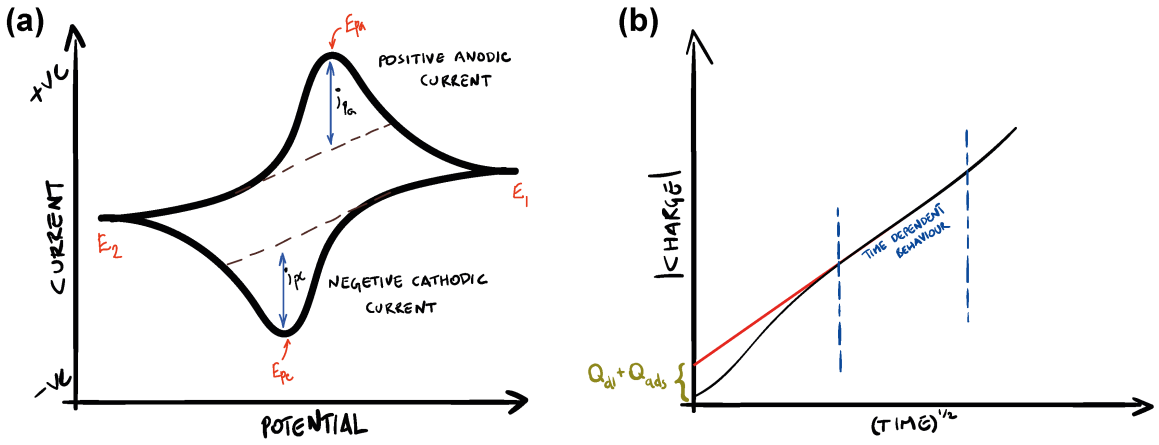

Figure 2.2: (a) Simplified schematic representation of a cyclic voltammogram. **(b)** Deduction of confined species charge and double layer charge: schematic representation.

Cyclic voltammetry studies reveal numerous information about the respective electron transfer involved reaction. For reversible redox couple, the peak potential difference can give an idea on the number of electrons involved in the reaction by the following equation (equation 3).

$$E_{pa} - E_{pc} = \frac{0.059}{n} \qquad \textbf{(Equation 3)}$$

(E_{pa}= anodic peak potential (V), E_{pc}= cathodic peak potential (V), n= number of electrons)

Scan rate is an important parameter which explains how fast the potential is scanned. It determines the length of the diffusion layer and, thereby, the current by the Randles-Sevick's relation (equation 4).[34] Information from Randles-Sevick's equation indicates whether the redox species is freely diffusing or more confined to the electrode during the reaction at the interface.[34]

$$i_{pc} = \left(2.69 \times 10^5\right) n^{\frac{3}{2}} A D^{\frac{1}{2}} \nu^{\frac{1}{2}} C \qquad \textbf{(Equation 4)}$$

(i_{pc}= peak current (A), n= number of electrons, A= area of electrode (cm^2), D= diffusion coefficient ($cm^2\ s^{-1}$), C= concentration (mole cm^{-3}), ν= scan rate ($V\ s^{-1}$))

Chronoamperometry:

As the name suggests, chronoamperometry is the measure of current as a function of time with a constant applied potential over the working electrode. Charge(Q) vs. time(t) relation also can be traced from the chronoamperometry experiment. This step potential technique is often used to study parameters such as active electrode surface area, diffusion coefficients, adsorbed charge. The current vs. time relation can be easily converted.[35]

$$i(t) = \frac{nFACD^{\frac{1}{2}}}{(\pi t)^{\frac{1}{2}}} \qquad \textbf{(Equation 5)}$$

(i= current (A), t= time (s), A= area of electrode (cm^2), D= diffusion coefficient ($cm^2\ s^{-1}$), C= concentration (mol cm^{-3}), n= number of electrons, F= Faraday constant(~96500 C))

$$Q_{total} = Q_t + Q_{dl} + Q_{ads} \quad \textbf{(Equation 6)}$$

(Q_{total}= total charge involved (C), Q_t= time dependent charge (C), Q_{dl}= double layer charge (C), Q_{ads}= adsorbed charge (C))

The total charge measured during the experiment could be from the faradic process, which is time-dependent according to Cottrell equation (equation 5), or it can be from the double layer as well as confined species near to electrode (equation 6). The Anson analysis plots Q vs. $t^{1/2}$ gives a linear region were the Cottrell equation follows. The graph could further provide a Y-intercept showing the sum of the double layer and confined charge (figure 2.2b)[47,48]. Besides, the surface coverage is calculated from this charge using equation 7.

$$Q_{ads} = nFA\tau_{max} \quad \textbf{(Equation 7)}$$

(Q_{ads}= adsorbed charge (C), n= number of electrons, F= Faraday constant (~96500 C), A= area of electrode (cm^2), τ_{max}= surface coverage (mol cm^{-2}))

Electrochemical Impedance Spectroscopy (EIS):

Impedance is the net opposition experienced by an alternative current (AC) flow, which includes resistance includes the contribution from resistive (real part- Z'), capacitive as well as inductive component (imaginary part- Z'') (figure 2.3a). EIS is an important experiment that will help us understand the whole electric circuit in the electrode-electrolyte interface region.

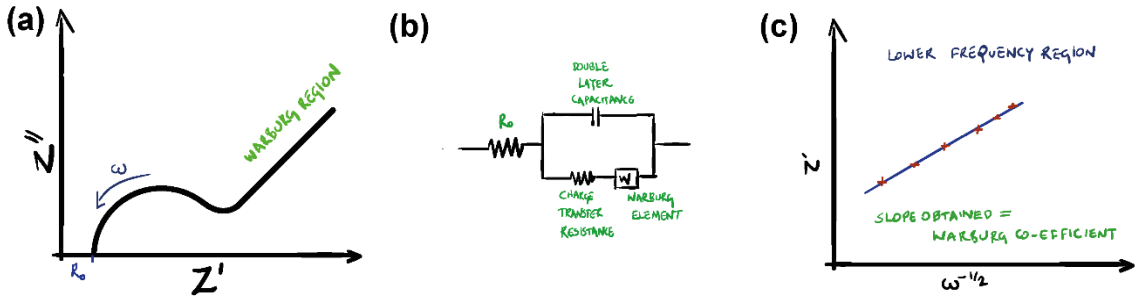

Figure 2.3: (a) Schematic representation of impedance profile for a simple circuit depicted in 'b'. **(b)** Circuit diagram. **(c)** Warburg coefficient deduction method.

A typical impedance profile which includes an electrode-electrolyte interface, solution resistance along with the diffusion component will be as in figure 2.3a. A circuit can be modelled for a particular impedance spectroscopy profile using ZSimpWin freeware software. Figure 2.3b shows a plausible circuit corresponding to the plot explained in figure 2.3a. Within the scope of this thesis, the EIS has specifically used to analyze the Warburg component since it indicates the diffusion process changes as the electrode material modification happens. Warburg coefficient is used to explain the phenomena as mentioned above, which essentially is the slope in a resistance component (Z') vs. the inverse square root of the AC frequency signal ($\omega^{-1/2}$) plot (figure 2.3c).[49,50]

Rotating Disk Electrode:

Rotating Disk Electrode (RDE) is a hydrodynamic technique that can give a lot of vital information about the electroactive species reaction kinetics. The setup includes a rotating motor shaft where the electrode is mounted, whose speed can be controlled to different RPMs.

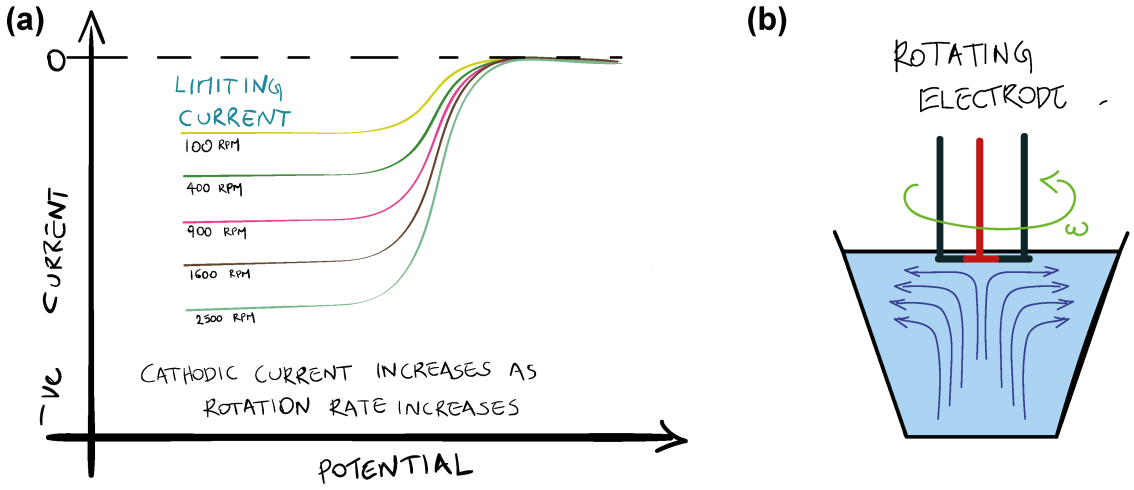

Figure 2.4: (a) Linear voltammogram showing limiting current. **(b)** RDE forced convection mass transfer: A schematic representation.

A linear scan voltammogram profile that sweeps from an initial potential to a final potential on a rotating working electrode at different RPMs can be used to analyze some of the crucial parameters involved in the reaction kinetics (figure 2.4a). The

electrode rotation mainly facilitates a constant supply of electroactive species towards the electrode surface (figure 2.4b), which helps to achieve a limiting current upon the linear voltammetry sweep. The particular profile is modelled using the Levich equation (equation 8).[20]

An important parameter that we used in this thesis the mass transfer coefficient (k_m). k_m has a unit of cm/s or cm^3. $s^{-1}.cm^{-2}$, where we can describe it as a net volume flow per second and per area. This parameter is also determined using this same RDE analysis with the help of the equation 9. k_m is defined as the product of the diffusion coefficient and inverse of double-layer length.[55-56]

$$i_l = 0.62nFAD^{\frac{2}{3}}\nu^{-\frac{1}{6}}C\omega^{\frac{1}{2}} \qquad \textbf{(Equation 8)}$$

$$k_m = \frac{D}{\delta} = 0.62D^{\frac{2}{3}}\omega^{\frac{1}{2}}\nu^{-\frac{1}{6}} = \frac{i}{nFAC} \qquad \textbf{(Equation 9)}$$

(k_m= mass transfer coefficient (cm s^{-1}), n= number of electrons, A= area of electrode (cm^2), δ= double layer length (cm), C= concentration (mol cm^{-3}), D= diffusion coefficient (cm^2 s^{-1}), F= Faraday constant (~ 96500 C), ν= scan rate (V s^{-1}), ω= rotation rate (rad s^{-1}))

2.3.2. *Material Characterization:*

Various material characterization techniques were used during the research, which was crucial to explain the formation of certain materials. Standard procedures were followed to do material characterization techniques. The instruments used for doing different characterization techniques are mentioned in table 2.2.

The unmodified CNT, P-CNT & N-CNT are subjected to different characterization methods such as attenuated total reflectance-infrared spectroscopy (ATR-IR), zeta potential measurement, Raman spectroscopy, X-ray photoelectron spectroscopy (XPS) and contact angle measurement. Powder samples were used to do the spectroscopy methods, i.e., ATR-IR, Raman & XPS. For the zeta potential measurement, 1 mg of particular sample dispersed in 2 ml of distilled water and 0.22-micrometer syringe filtered solution is used. In the case of contact angle (of water)

measurement, the particular sample is dispersed in isopropyl alcohol (IPA) and drop cast and dried on a 0.5cm x 0.5cm carbon sheet to get a fine uniform layer.

Table 2.2: Instruments used for various material and electrochemical characterization experiments.

Technique	Instrument
Electrochemical analyses	VMP-300 Electrochemical Work Station (Biologics), PARSTAT MC (Amatek)
Rotating Disk Electrode	PARSTAT MC (Amatek)
IR spectroscopy	ATR-FTIR (Bruker Platinum ATR Spectrometer System)
Raman Spectroscopy	LAB-RAM HR 800
Zeta Potential Measurement	Zetasizer Nano ZS90 Analyzer (Malvern)
Contact Angle Measurement	Contact Angle Instrument [HO-IAD-CAM01] (HOLMARC Opto-Mechatronics)
X-Ray Photo-electron Spectroscopy	Thermo Scientific K-alpha^{+} spectrometer (AL-Kα as excitation source)

.

2.4. Battery Fabrication:

All the battery experiments were carried out in static mode. The battery was fabricated in a two-compartment cell configuration separated by a cation exchange Nafion® 212 polymer electrolyte membrane. Anodic half-cell is fabricated by immersing the electrode in electrolyte mixture containing 0.2 M $FeCl_2$, 1M triethanolamine, and 1.5 M KOH, whereas cathodic half-cell contains 0.2 M ferricyanide dissolved in 3 M KOH. A Toray carbon paper coated (2cm x 2cm) with positively charged carbon nanotube (P-CNT), negatively charged CNT (N-CNT), and unmodified CNT was used as the driving electrode for both half cells. The CNT ink was prepared by mixing its required amounts with 5% binder solution in 2-propanol followed by ultrasonication for 1 hour. The ink was then brush coated over the Toray carbon paper at a loading of 3 mg/cm^2. The galvanostatic charge/discharge experiments were carried out at different current rates.

CHAPTER 3

RESULTS & DISCUSSION

Architectural components of the proposed iron(II)triethanolamine-ferricyanide battery are shown in (figure 3.1), and it consist of the negative electrode immersed in a mixture of $FeCl_2$ (0.2 M), triethanolamine (1 M) and KOH (1.5 M) solution (details are provided in the section 2.4) as the anodic half-cell, Nafion® 212 membrane as the separator and $[Fe(CN)_6]^{3-}$ (0.2 M) dissolved in KOH (3 M) as the cathodic half-cell.

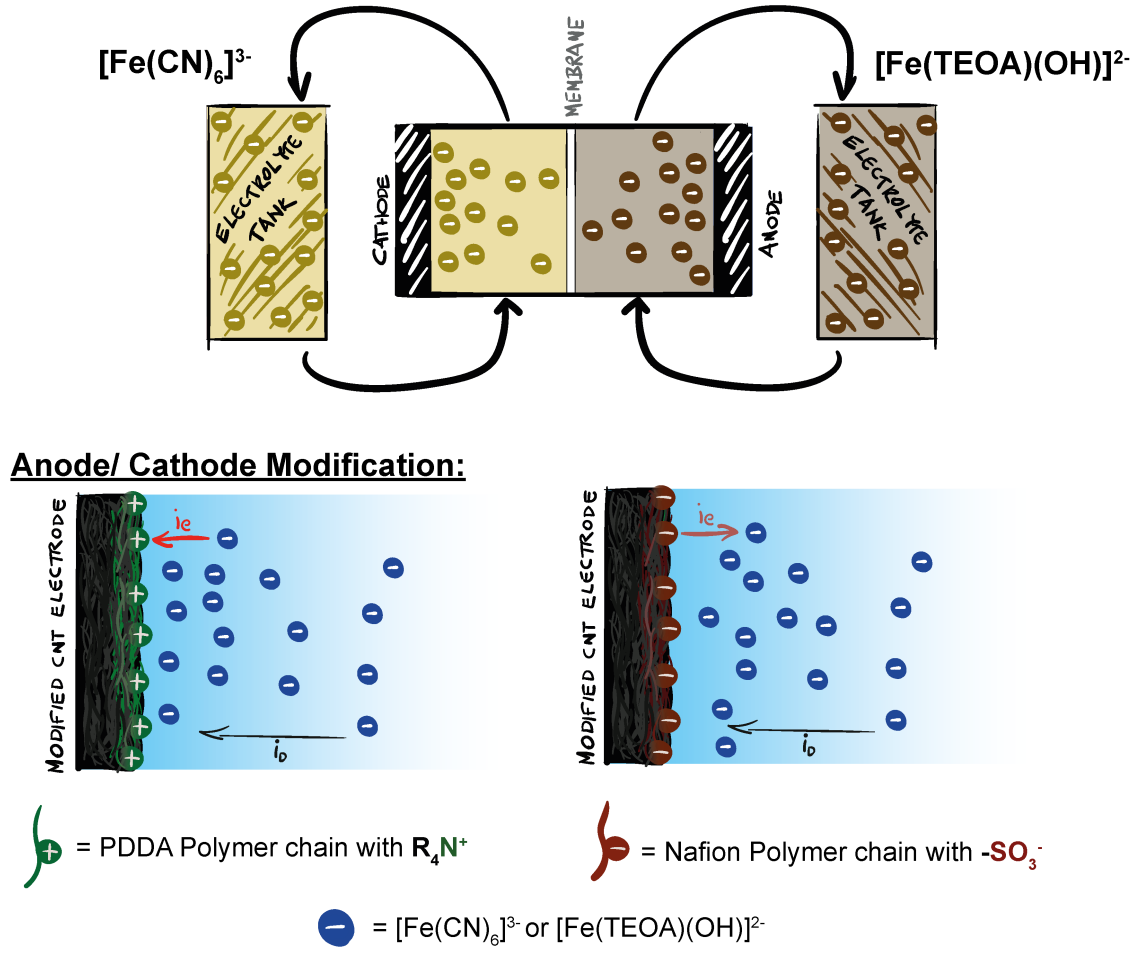

Figure 3.1: The anodic half cell is iron(III/ II)triethanolamine and cathodic half cell is ferricyanide/ ferrocyanide separated by a Nafion 212 membrane. The interfacial chemistry of driving electrode is tuned to positive and negative (experimental section 2.4.1) respectively to achieve Coulombic attraction and repulsion towards negatively charged electroactive species, i.e. $[Fe(TEOA)(OH)]^{2-}$ and $[Fe(CN)_6]^{3-}$. i_D is the diffusion current contribution and i_e is electrostatic current contribution.

Carbon nanotube (CNT) coated Toray carbon paper was employed as the working electrodes for both iron (II)triethanolamine complex and ferricyanide half-cells and the surface charge of CNT electrode was tuned from positive to negative (as discussed in the section 2.2.1) to respectively exert electrostatic attraction and repulsion towards negatively charged iron(II)triethanolamine & ferricyanide complexes (figure 3.1) .[40-46]

Ferricyanide/Ferrocyanide cathodic redox reaction: *(+0.48 V vs. SHE)*

$$[\mathbf{Fe(CN)_6}]^{3-} + \mathbf{e}^- \rightleftharpoons [\mathbf{Fe(CN)_6}]^{4-} \quad \textbf{(Equation 10)}$$

Fe(III/ II)triethanolamine (TEOA) anodic redox reaction: *(-0.86 V vs. SHE)*

$$[\mathbf{Fe(TEOA)OH}]^- + \mathbf{e}^- \rightleftharpoons [\mathbf{Fe(TEOA)(OH)}]^{2-} \quad \textbf{(Equation 11)}$$

Total cell reaction: *(Potential Difference: 1.34 V)*

$$[\mathbf{Fe(CN)_6}]^{3-} + [\mathbf{Fe(TEOA)(OH)}]^{2-} \rightleftharpoons [\mathbf{Fe(CN)_6}]^{4-} + [\mathbf{Fe(TEOA)OH}]^- \quad \textbf{(Equation 12)}$$

An iron(II)triethanolamine-ferricyanide battery configuration is feasible because of the positive electromotive force between ferrocyanide/ferricyanide and iron(II/III)triethanolamine redox reactions in chosen electrolytes, figure 3.2b, and the battery half-cell and full cell chemistries are in accordance with equations 10-12.[14] With an unmodified carbon nanotube (CNT) electrode as the driving electrode for ferricyanide, the half-cell electrode polarization with respect to a common reference electrode suggests that ferricyanide half-cell limit the overall device performance compared to a well-known inner-sphere mechanistic redox species such as Zn/ Zn^{2+} (figure 3.2a).[16,36,37] Since ferricyanide and iron(II)triethanolamine are reversible electron donor/acceptor, their reaction velocity is dominantly transport controlled, making it independent of inherent electrode characteristics, area normalized voltammograms on Au, Pt, and glassy carbon (GC) electrodes, figure 3.2c, 3.2d. Near the electrode surface, spatial structuring of solution force simple diffusion to dominate the transport phenomena even under convective fluid flow that, in turn, pose unique challenges to utilize the full potential of the molecule either by the electrode (electrocatalysis) or fluid characteristics (fluid flow).[38,39]

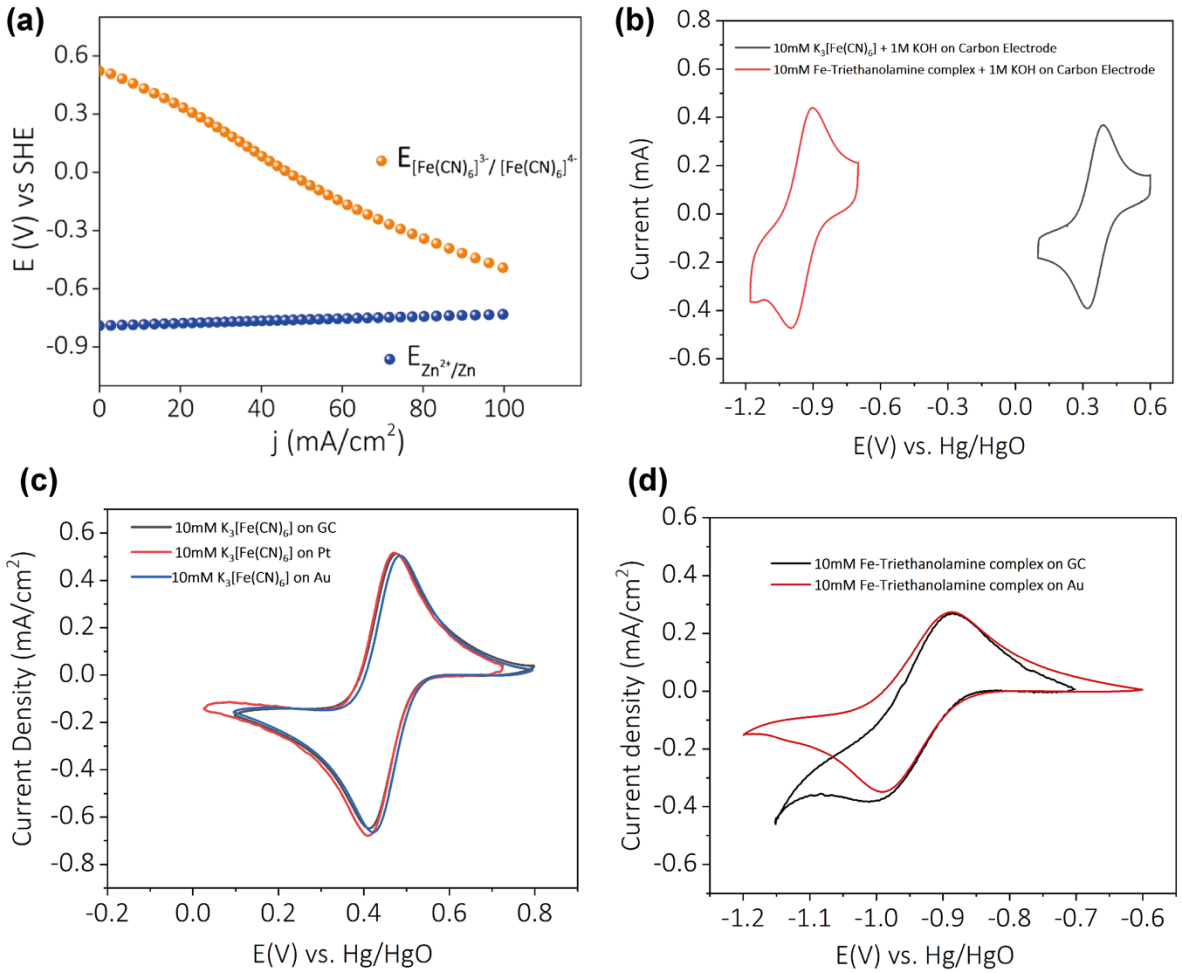

Figure 3.2: (a) Half-cell electrode polarization of Zn/Zn^{2+} (an inner-sphere electron transfer species) by immersing a Zinc foil in 0.1M $ZnSO_4$ and $[Fe(CN)_6]^{3-}$/ $Fe(CN)_6]^{4-}$ (an outer-sphere electron transfer species) on a carbon electrode. **(b)** Cyclic voltammogram showing the potential difference between iron(II/III)triethanolamine redox couple in 1M KOH electrolyte and $[Fe(CN)_6]^{3-}$/ $Fe(CN)_6]^{4-}$ redox couple in 1M KOH. **(c)** Cyclic voltammogram of $[Fe(CN)_6]^{3-}$/ $Fe(CN)_6]^{4-}$ on GC, Pt and Au working electrodes. **(d)** Cyclic voltammogram of iron(II/III)triethanolamine on GC and Au working electrodes.

We exploit the negative charge on ferricyanide and iron(II)triethanolamine redox species to amplify its interfacial electrochemistry, and consequently, its battery performance. To do so, we have activated Coulombic forces at the driving carbon nanotube (CNT) electrode/electrolyte interface by covering CNT electrode with polymeric species such as polydiallyldimethylammonium chloride (PDDA) and Nafion® perfluorinated resin to make it positively and negatively charged respectively (please refer the discussion below and section 2.2.1 for more details).[40-46] In line with this anticipation, with a positively charged carbon nanotube (P-CNT) electrode, the

redox currents are significantly amplified (cyclic voltammogram, red trace, figure 3.3) with a decrease in peak potential separation (ΔE_p) for the peak pair II, II' compared to unmodified CNT (table 3.1).

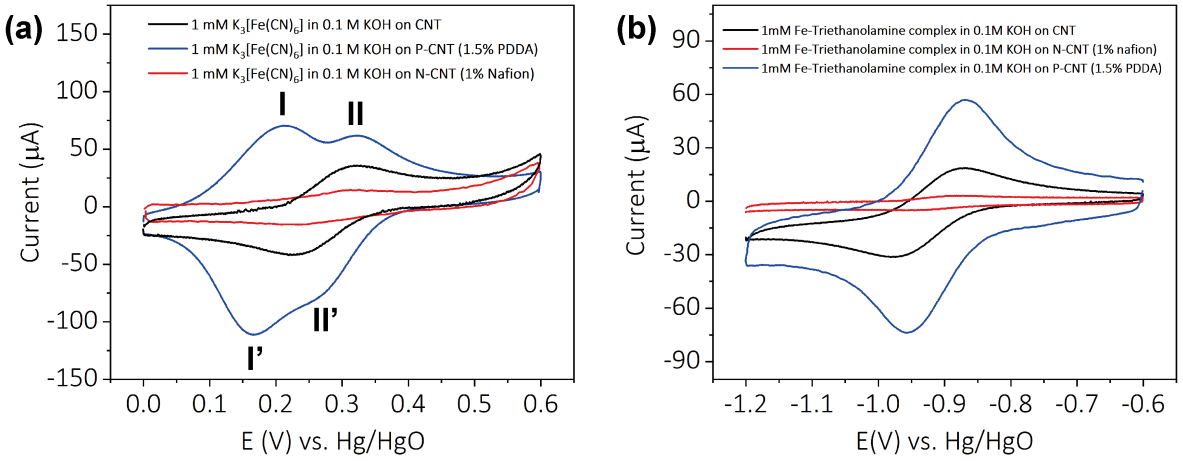

Figure 3.3: (a) CV studies of 1mM $K_3[Fe(CN)_6]$ in 0.1M KOH on CNT, P-CNT & N-CNT, **(b)** CV studies of 1mM Iron(III)-Triethanolamine complex in 0.1M KOH on CNT, P-CNT & N-CNT.

Table 3.1: ΔE_P values extracted from cyclic voltammogram (from figure 3.3).

Material	ΔE_P ($[Fe(CN)_6]^{3-}$/ $Fe(CN)_6]^{4-}$)	ΔE_P (iron(II/III)triethanolamine)
CNT	83 mV	84 mV
P-CNT	35 mV (I / I'), 59 mV (II / II')	56 mV
N-CNT	100 mV	89 mV

Since the electrode loadings are the same in all three cases, the faradaic behavior depends upon the transport velocity of the reacting molecules towards the electrode surface. The positively charged polymer (PDDA) is responsible for electrostatically attracting ferricyanide as well as iron(III)triethanolamine towards the electrode surface, leading to an electrostatic current contribution parallel to the diffusion current (figure 3.1). Therefore, activation of Coulombic forces at the interface leads to gated molecular transport in the reaction zone, which can be exploited to trigger directional electrostatic current over the diffusion current. In this all iron-based redox flow battery, this gated molecular flux is capable of almost doubling the volumetric energy density without compromising the power capability by extending the

concentration polarization regime. The redox activity decreased noticeably (red trace, figure 3.3, table 3.1) with a negatively charged CNT (N-CNT), pointing the origin of this to Coulombic forces.

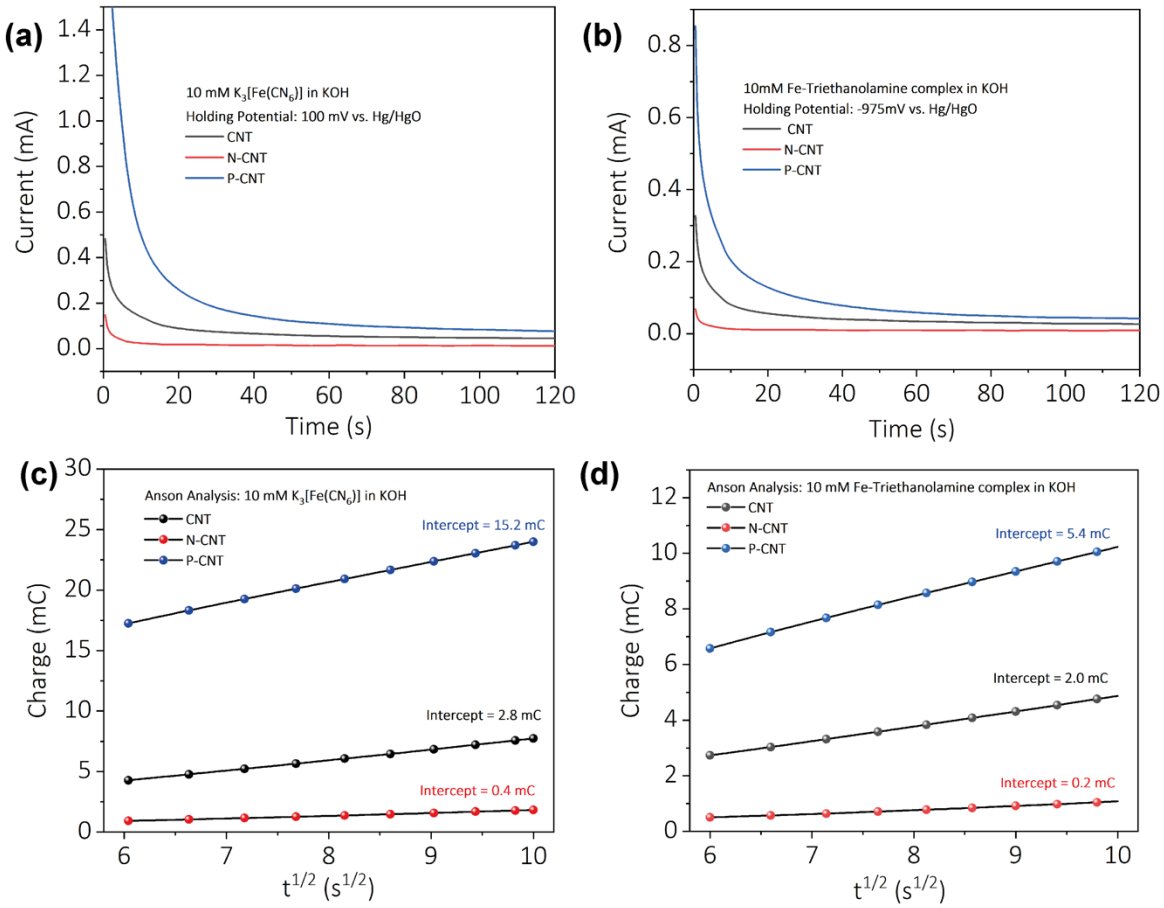

Figure 3.4: Chronoamperometry investigation on **(a)** 10mM $K_3[Fe(CN)_6]$ in 1M KOH with a holding potential 100mV vs. Hg/ HgO & **(b)** 10mM iron(III) triethanolamine complex in 1M KOH with a holding potential -975mV vs. Hg/ HgO on CNT, P-CNT & N-CNT. Corresponding Anson plots: **(c)** $K_3[Fe(CN)_6]$ & **(d)** iron(III) triethanolamine complex.

In line with these, the chronoamperometric traces in the diffusion-limited region (at a potential of 100mV in 10mM ferricyanide & -975mV in 10mM iron(III)triethanolamine with respect to Hg/HgO) demonstrated noticeably higher currents on P-CNT compared to unmodified and N-CNT electrodes, figure 3.4a, 3.4b, reflecting substantially higher mass transport of negatively charged ferricyanide & iron(III)triethanolamine towards the former electrode. The Anson plot (charge vs. square root of time, section 2.2.2) with ferricyanide & iron(III)triethanolamine clearly indicates that the overall charge transferred is higher on the P-CNT electrode (figure

3.4c, 3.4d). The intercept of this linear plot reflects the charge contribution from adsorbed species & double layer (table 3.2).[47,48] The charge difference will provide the contribution of charge only due to adsorption on the P-CNT electrode compared to the unmodified CNT electrode, (a similar calculation gives the decrement of charge contribution due to N-CNT) (figure 3.4c, 3.4d, table 3.3). Therefore, the positive surface charge on the driving electrode pre-concentrates the negatively charged ferricyanide & iron(III)triethanolamine species at its interface and significantly improves the overall transport velocity of the reversible species within the diffusion layer.

Table 3.2: Total time independent charge transfer values, (i.e. double layer charge contribution (Q_{dl}) & adsorbed charge contribution (Q_{ads}) values extracted from figure 3.4)

Material	$Q_{dl} + Q_{ads}$ (mC)	
	$[Fe(CN)_6]^{3-}/ Fe(CN)_6]^{4-}$	Iron(II/III)triethanolamine
CNT	2.8	2.0
P-CNT	15.2	5.4
N-CNT	0.4	0.2

Table 3.3: Surface coverage change of the electroactive redox species on P-CNT and N-CNT compared to unmodified CNT.

Material	Surface Coverage Difference compared to CNT (mol/cm^2)	
	$[Fe(CN)_6]^{3-}/ Fe(CN)_6]^{4-}$	Iron(II/III)triethanolamine
P-CNT	6.5×10^{-7} increased	1.8×10^{-7} increased
N-CNT	1.3×10^{-7} decreased	1.0×10^{-7} decreased

In order to strengthen our claim, we prepared the positively charged electrode by introducing positively charged quaternary ammonium groups on the CNT (see experimental section 2.2.1 for the synthetic procedure).

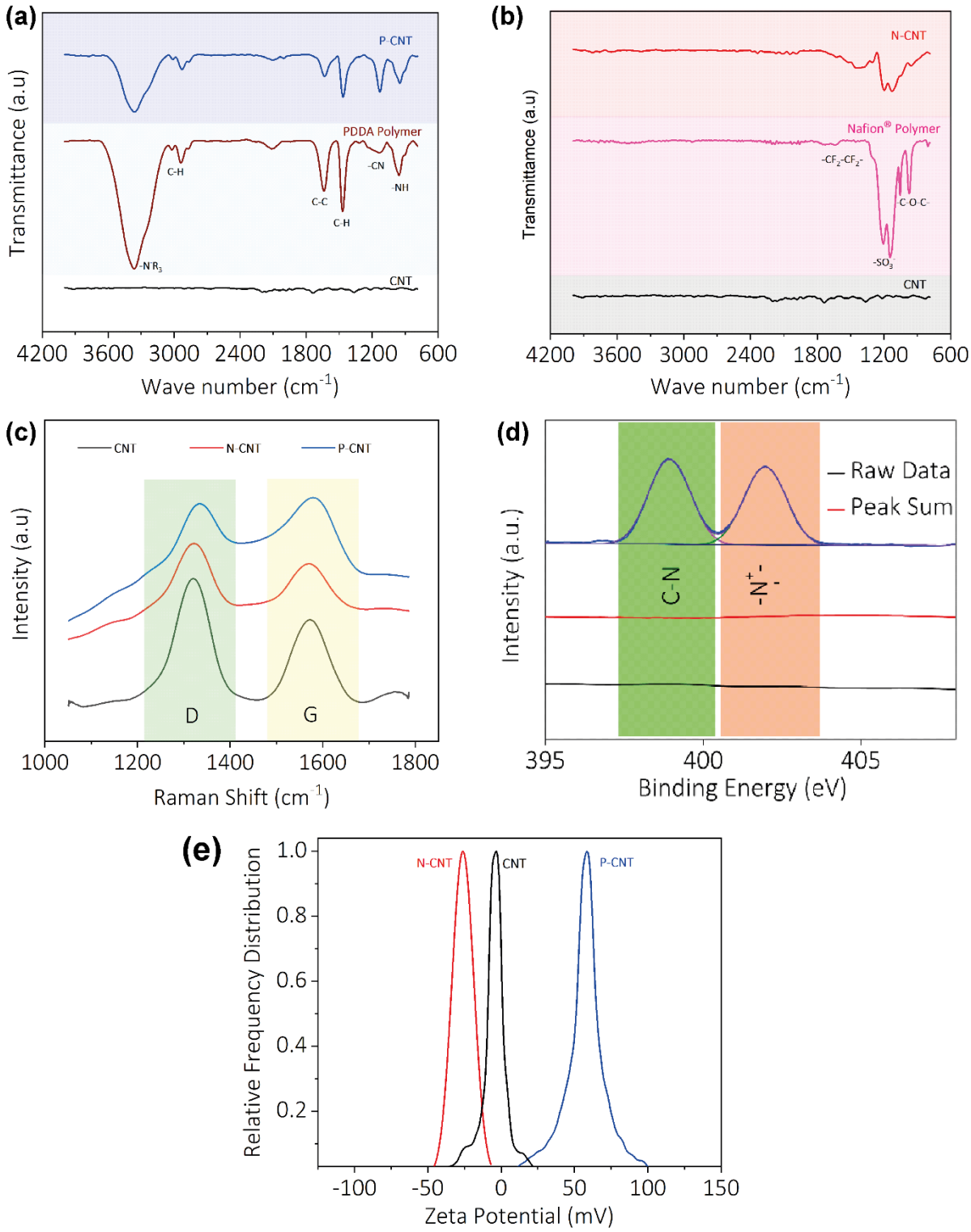

Figure 3.5: (a) ATR-IR spectra of P-CNT and individual components. **(b)** ATR-IR spectra of N-CNT and individual components. **(c)** Raman spectra of unmodified CNT, P-CNT and N-CNT. **(d)** N 1s XPS spectra of unmodified CNT, P-CNT and N-CNT. **(e)** Zeta potential measurements of unmodified CNT, P-CNT and N-CNT.

The newly synthesized positive charged CNT was characterized thoroughly by IR and Raman spectroscopy to confirm the introduction of quaternary ammonium groups on CNT before the electrochemical experiments as per section 2.3.2 (figure 3.5a, 3.5b, 3.5c). Interestingly, when the newly synthesized P-CNT material was used as electrodes in the battery configuration, the performance was enhanced as compared to the unmodified CNT (figure 3.13a).

Taken together, these point to the fact that activation of Coulombic forces at the interface generates an electrostatic current contribution in addition to the diffusion current. When the electrode surface is positive, (significantly) higher charge under the curve (Figure 3.3, Figure 3.4a, 3.4b, and Table 3.2) signal that electrostatic current contribution is parallel to the diffusion current. A diametrically opposite behaviour observed when the electrode surface is negatively charged (by introducing SO^{3-} at the CNT surface, which is visible from figures 3.5b, 3.5c explains the IR and Raman spectroscopic data) reflects the fact that electrostatic current is opposite to the diffusion current. Therefore, Coulombic forces at the interface play a dominant role in directing molecular transport of ionic redox species within the reaction zone.

Electrochemical impedance spectroscopy (EIS) was employed to investigate the interfacial effects of activating Coulombic forces, (figure 3.6b, 3.6c). EIS data was fitted with an equivalent circuit (figure 3.6a) to model the interface.

Table 3.4: Warburg coefficient values extracted from EIS Data (from figure 3.6).

Material	Warburg Coefficient	
	$[Fe(CN)_6]^{3-}$/ $Fe(CN)_6]^{4-}$	Iron(II/III)triethanolamine
CNT	233	128
P-CNT	67	46
N-CNT	363	156

In order to investigate the effects of Coulombic forces on the electrode towards the transport velocity of redox species, the real part of the impedance (Z′) was plotted against the inverse of the square root of frequency in the lower frequency region, (figure 3.6d, 3.6e), and it shows that slope corresponding P-CNT electrode is the

lowest and N-CNT is the highest. The slope of this plot is known as the Warburg coefficient (σ), which is inversely related to the transport velocity of the redox species towards the electrode.[49,50]

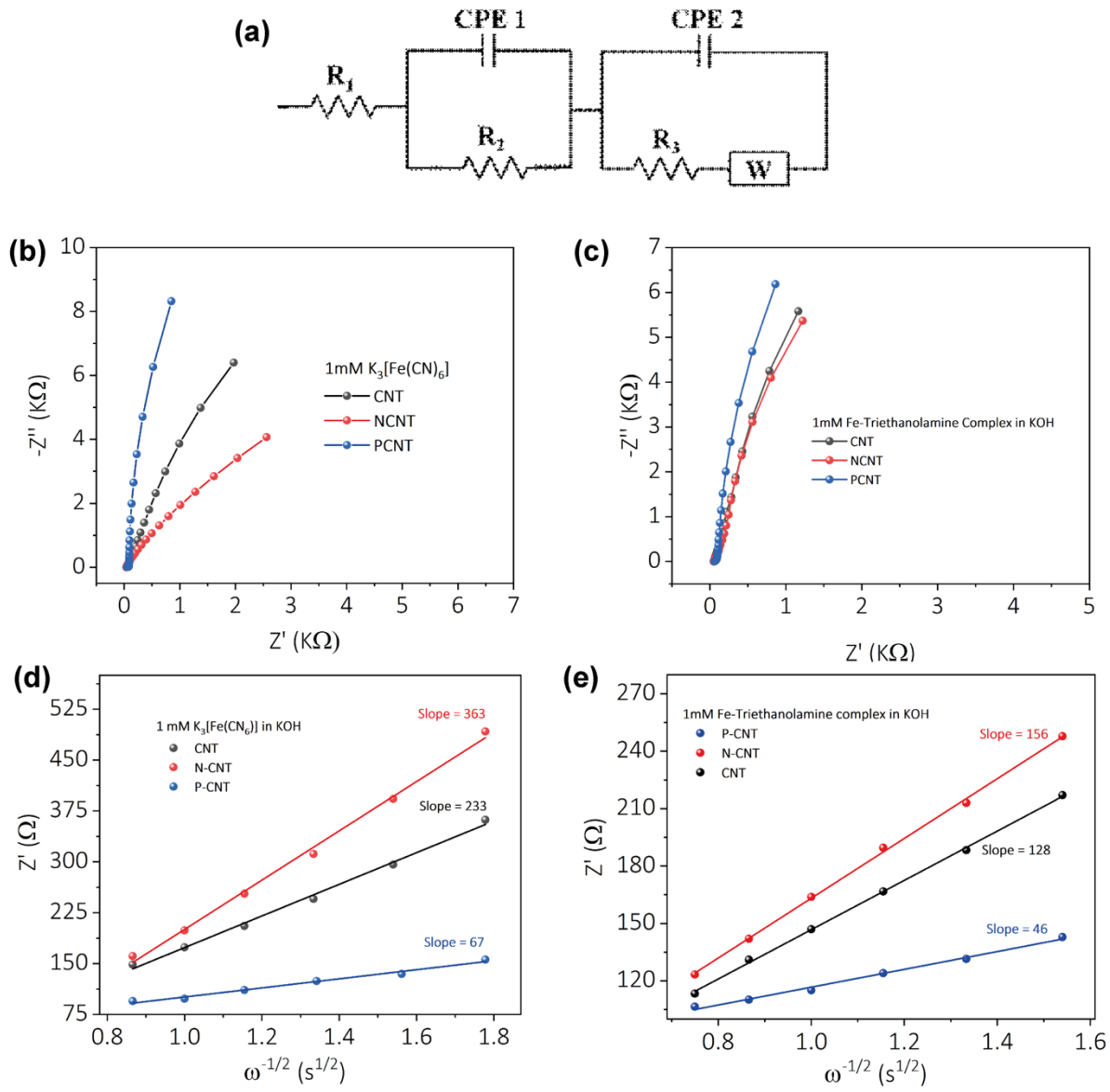

Figure 3.6: (a) Equivalent circuit diagram for 'b' and 'c'. Nyquist plot of unmodified CNT, P-CNT & N-CNT with **(b)** 1 mM of $[Fe(CN)_6]^{3-}$ dissolved in 0.1 M KOH and **(c)** 1 mM iron(III)triethanolamine complex in 0.1 M KOH. The plot of real part of impedance (Z') as a function of inverse square root of angular frequency in the Warburg region extracted from **(d)** $[Fe(CN)_6]^{3-}$ EIS data and **(e)** iron(III)triethanolamine complex EIS data.

The lower slope with P-CNT shows that the positive charge on the electrode significantly enhances the transport velocity of ferricyanide & iron(III)triethanolamine (table 3.4). On the other hand, the transport velocity with N-CNT decreases even

below that of unmodified CNT due to the negative charge on the former electrode. The lower Warburg coefficient with a P-CNT electrode compared to an N-CNT electrode reflect the fact that Coulombic forces can be exploited to gate the molecular transport of ionic redox species within the reaction zone. When the electrode charge is positive, it exerts an attractive force on negatively charged ferricyanide & iron(III)triethanolamine complex leading to an amplification in its redox behavior and vice versa. Therefore, it can be concluded that the current amplifications observed in figure 3.3 with the P-CNT electrode is primarily due to an electrostatic current contribution parallel to diffusion current (figure 3.1). On the other hand, with the N-CNT electrode, the decrease in redox current is mainly due to an opposing electrostatic current with respect to diffusion current, figure 3.3, and figure 3.1.

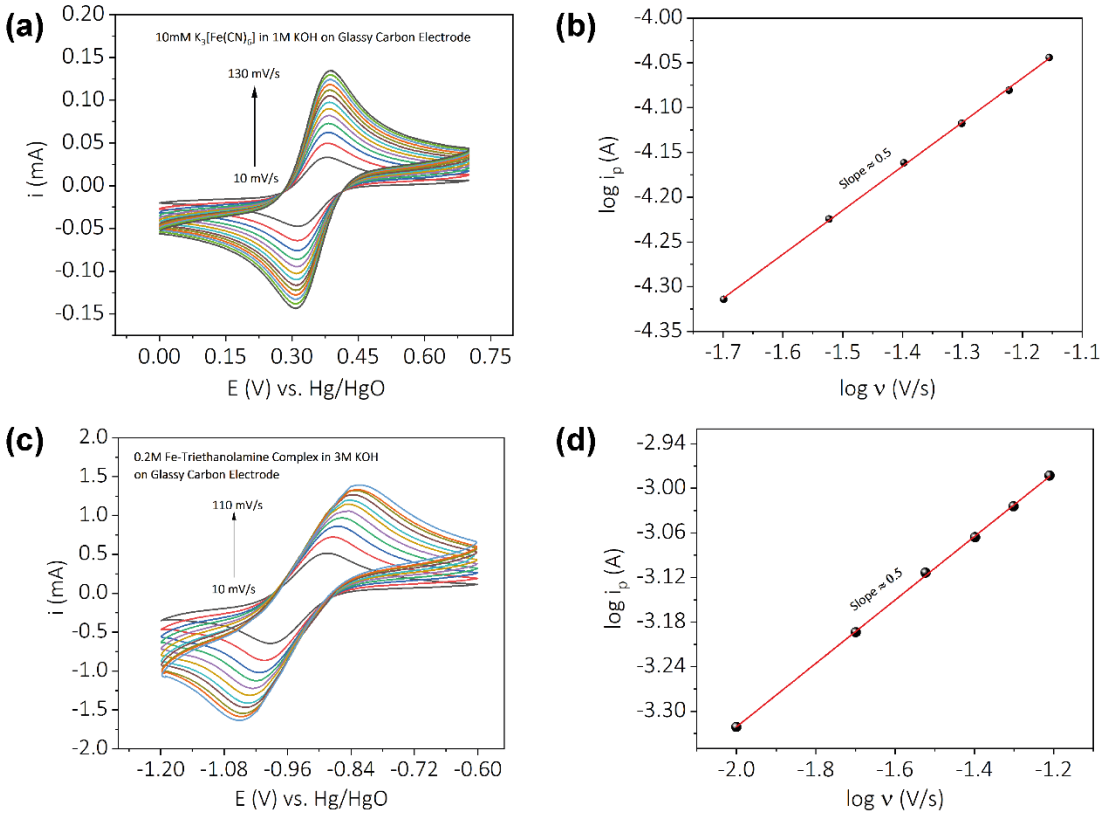

Figure 3.7: (a) Cyclic voltammogram studies of 10mM $K_3[Fe(CN)_6]$ in 1M KOH by varying scan rate on GC working electrode. **(b)** $\log(i_p)$ vs. $\log(\nu)$ relation deduced from 'a'. **(c)** Cyclic voltammogram studies of 0.2 M $K_3[Fe(CN)_6]$ in 3M KOH by varying scan rate on GC working electrode. **(b)** $\log(i_p)$ vs. $\log(\nu)$ relation deduced from 'c'.

It should be noted that the voltammograms on P-CNT demonstrate multiple set of peaks (Figure 3.3a) and the first peak pair at more negative potentials (peak pair I,

I') is attributed to confined ferricyanide in PDDA polymer chains on P-CNT, (the scan rate dependent cyclic voltammograms, Figure 3.8a). The plot of log (I_p) vs. log (ν) yielded a slope of ~0.9, suggesting the situation resembling a thin layer diffusion (Figure 3.9b). The peak pairs I, I' and II, II' evidenced peak-potential separations of ~35 mV and ~60 mV respectively, demonstrating that the former arises from the confined ferricyanide species. This corroborates the fact that the positive charge on the P-CNT electrode can pre-concentrate negatively charged ferricyanide species at its interface, as discussed for the Anson plot (Figure 3.4c, table 3.2, 3.3). By further analysis by rotating disk electrode (RDE) technique shows persistence of a peak even with forced convection points the fact that it is from confined ferricyanide species (figure 3.10b). The second peak pair (II, II') close to the formal potential 175 mV with respect to Hg/ HgO on the P-CNT electrode correspond to freely diffusing ferricyanide redox species as similar features existed on carbon electrode (Figure 1c). The scan rate dependence of the peak pair II, II' on the P-CNT electrode demonstrates a majorly diffusion-controlled behavior with a log (i_p) vs. log (ν) slope of ~0.6 (figure 3.9a). The plot of log (i_p) vs. log (ν) of scan rate for bare carbon electrode demonstrated similar diffusion-controlled characteristics with a slope of ~0.5 (Figure 3.7a, 3.7b).

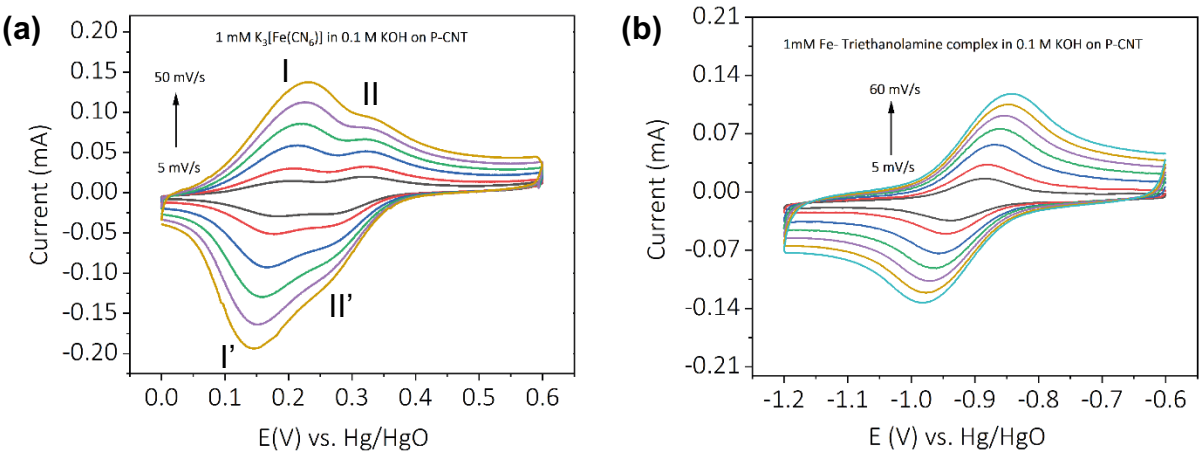

Figure 3.8: (a) CV of 1mM $K_3[Fe(CN)_6]$ in 0.1M KOH on P-CNT at different scan rates, **(b)** CV studies of 1mM Iron(III)triethanolamine complex in 0.1M KOH on P-CNT at different scan rates.

Although in the case of iron(III)triethanolamine complex, the extra set of peaks are not visible. Presumably, due to less potential difference between the set of peaks and correspondingly masked by the regular peak. The log (I_p) vs. log (ν) plot deduced

from the scan rate dependence studies gave a slope of ~0.6 demonstrates the reaction is controlled mostly due to diffusion (figure 3.8b, 3.9c) of iron(III)triethanolamine species. The concentration of negatively charged iron(III)triethanolamine species on P-CNT is again established further to Anson analysis (figure 3.4d, table 3.2, 3.3). The similar experiment responses over regular carbon electrode gave a slope ~0.5 concludes no confined species contribution whatsoever compared to the P-CNT (figure 3.7c, 3.7d).

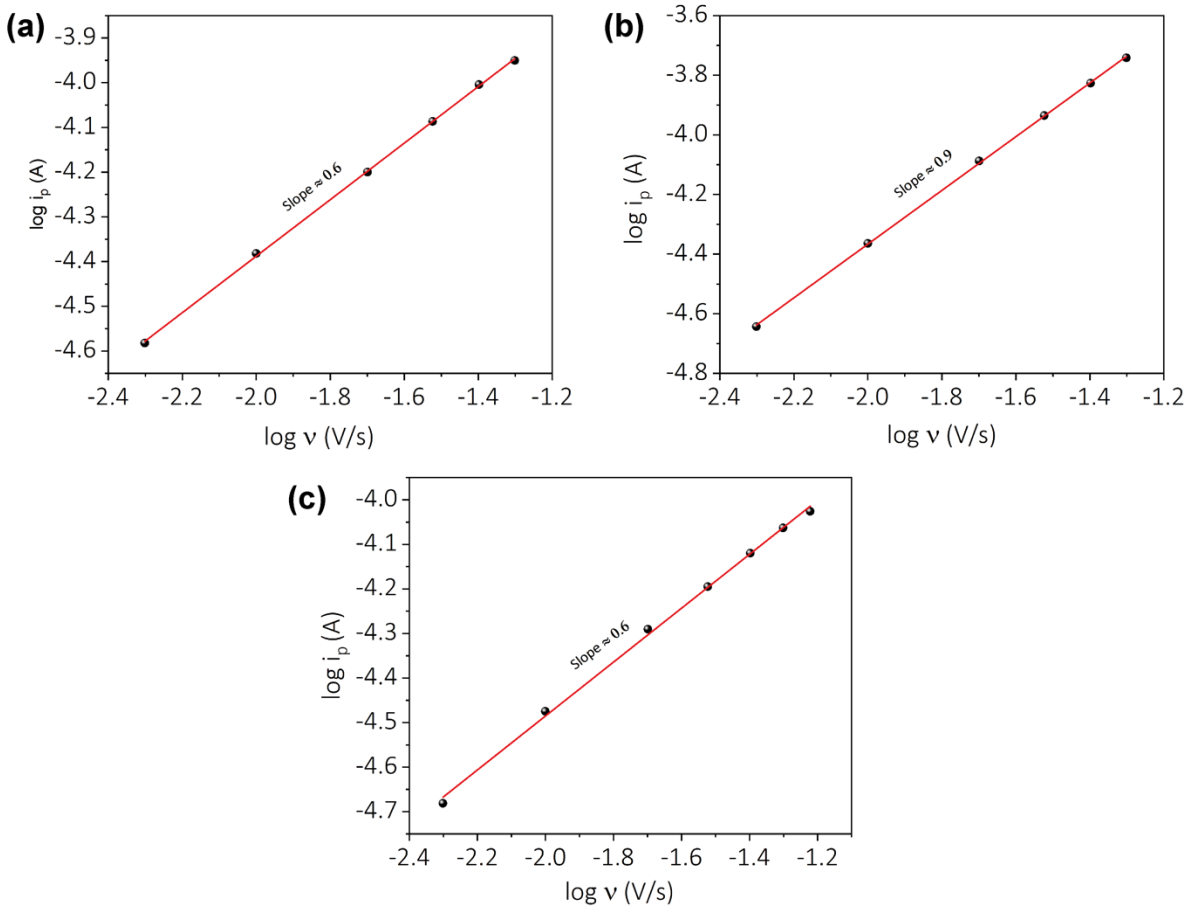

Figure 3.9: (a) log(i_p) vs. log(ν) relation deduced from **II / II'** set of peaks from figure 3.8a. **(b)** log(i_p) vs. log(ν) relation deduced from **I / I'** set of peaks from figure 3.8a. **(c)** log(i_p) vs. log(ν) relation deduced from from figure 3.8b set of cyclic voltammograms.

The rotating disk electrode (RDE) measurements shows the current increases with rotation rate (figure 3.10) and also noticeably higher currents on P-CNT compared to N-CNT and unmodified CNT even under forced convection reflect that the flux towards P-CNT is inherently higher due to Coulombic attraction (Figure 3.11a, 3.11c). Typically for aqueous media under forced convection, the thickness of the Prandtl

layer or hydrodynamic boundary layer is ~10 fold larger than the diffusion layer.[30,31] This indicates the contribution of convection near the electrode surface is negligible, and the major mode of transport is by simple diffusion. The peak in the rotating disk electrode (RDE) results support the fact that there is a contribution from the confined species over P-CNT material (figure 3.10e).

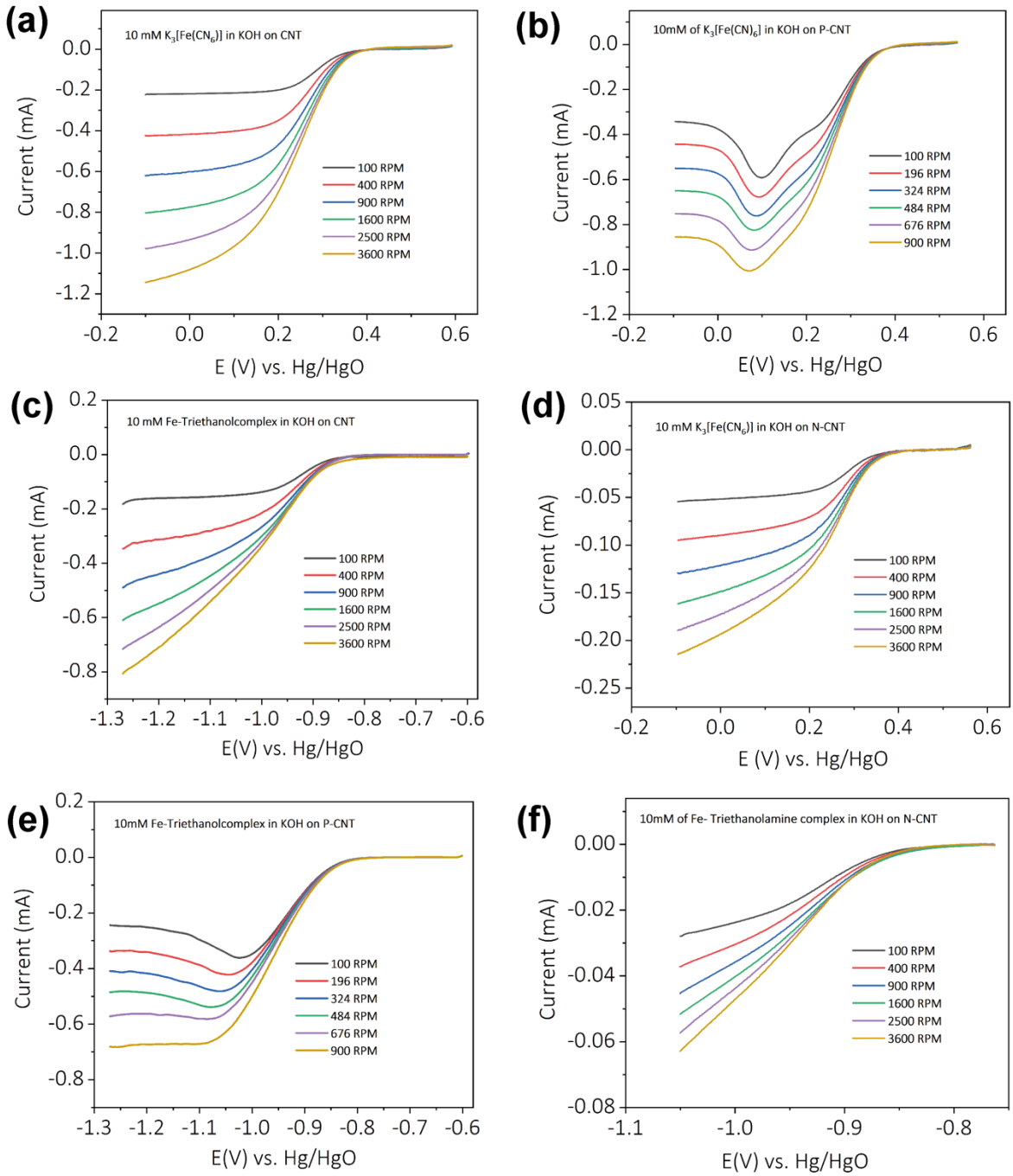

Figure 3.10: Linear scan voltammogram of respective studies on an RDE setup at different rotation rates: **(a)** 10mM $K_3[Fe(CN)_6]$ in 1M KOH on CNT, **(b)** P-CNT, **(c)** N-CNT & **(d)** 10 mM Iron(III)triethanolamine complex in 1M KOH on CNT, **(e)** P-CNT, **(f)** N-CNT.

Therefore, the increase in the limiting current in the P-CNT electrode compared to other electrodes even under convective fluid flow is due to the overall increase in transport velocity of molecules due to electrostatic attraction exerted by a positively charged electrode on negatively charged ferricyanide as well as iron(III)triethanolamine species. This is substantiated by extracting mass transfer coefficient (k_m) [55,56] from limiting currents (please refer section 2.3.1- Rotating Disk Electrode for more details) in figure (3.11b, 3.11d), which demonstrate ~1.5 times higher value with P-CNT electrode compared to unmodified electrode even under forced convection.

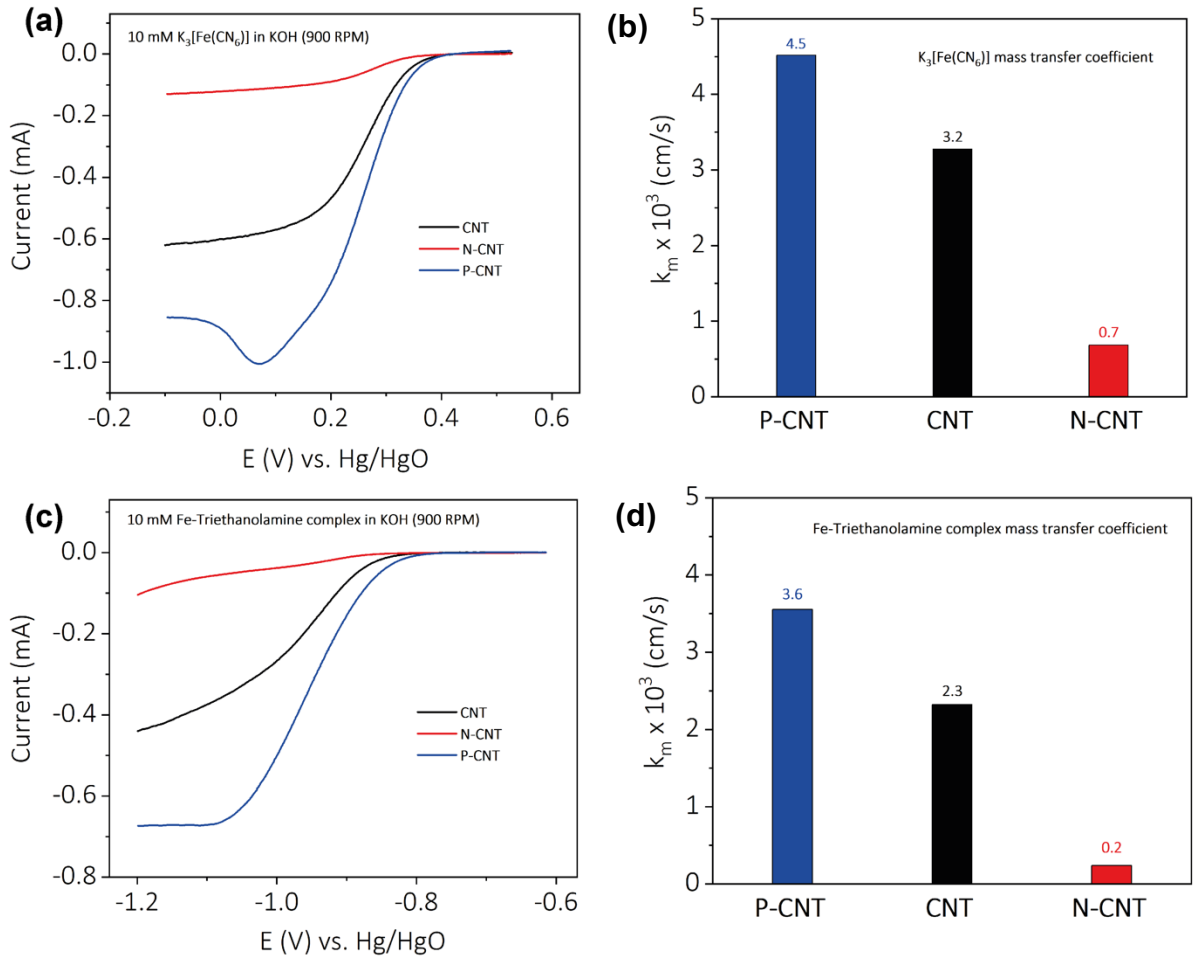

Figure 3.11: (a) LSV data in RDE setup at 900 RPM of 10mM $K_3[Fe(CN)_6]$ on CNT, N-CNT & P-CNT. **(b)** Mass transfer coefficient deduced for $K_3[Fe(CN)_6]$ from figure 'a' at 900 RPM. **(c)** LSV data in RDE setup at 900 RPM of 10mM Iron(III)triethanolamine complex on CNT,N-CNT & P-CNT. **(d)** Mass transfer coefficient deduced for Iron(III)-Triethanolamine complex from figure 'c' at 900 RPM.

To further strengthen our claim, we also carried out the contact angle measurements to check the wettability near the electrode surface. We can see that the P-CNT shows a higher contact angle compared to the N-CNT. The contact angle of the N-CNT electrode was lower than P-CNT and unmodified CNT electrodes (figure 3.12a, 3.12b, table 3.5). Therefore, the incorporation of PDDA on CNT does not change the wettability of electrodes noticeably, however, the presence of SO^{3-} rich functionalities in N-CNT does (figure 3.12c, table 3.5). Based upon the contact angle measurements, one would expect N-CNT to show higher performance because of its better wettability but the experimental results (Cyclic voltammetry, RDE figures) are opposite with P-CNT showing the superior performance.

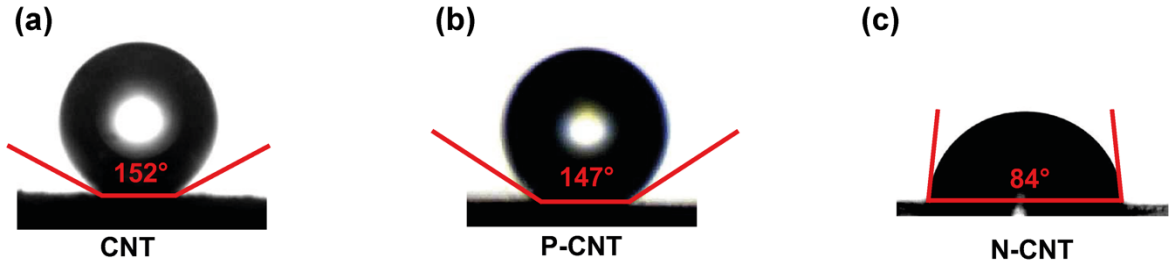

Figure 3.12: Contact angle measurement of water drop on **(a)** CNT, **(b)** P-CNT & **(c)** N-CNT material surface.

Table 3.5: Contact angle (of water) measurement values, Zeta potential measurement values and I_D/I_G ratio deducted from Raman spectra for unmodified CNT, P-CNT & N-CNT materials.

Material	Contact Angle	Zeta Potential	I_D / I_G ratio
CNT	152°	-4 mV	1.45
P-CNT	147°	58 mV	0.83
N-CNT	84°	-26 mV	1.54

These results further demonstrate that activation of Coulombic forces at the interface can amplify the interfacial electrochemistry of ionic redox species, which will be beneficial to boost its battery characteristics, as demonstrated below.

Positively and negatively charged carbon nanotubes (CNTs) were made by covering CNT with polydiallyldimethylammonium chloride (PDDA) [40-43] and Nafion®

perfluorinated resin,[45,46] respectively (please refer experimental section 2.2.1 for more details). Their surface charges are confirmed to be positive and negative, respectively, by zeta potential measurements (Figure 3.5e). ATR-FTIR spectra show the presence of PDDA and CNT features in positive CNT (P-CNT) and Nafion® presence in negative CNT (figure 3.5a, 3.5b). Raman spectra demonstrate the presence of D and G bands in all the compounds, and the I_D/I_G ratios indicate the effectiveness of the functionalization (figure 3.5c, table 3.5). D band reflects the defect density, whereas the G band defines the sp^2 moieties present in CNT.[51,52] The change in the ratio of I_D and I_G illustrates the functionalization of the multi-walled CNT (table 3.5). The lower and higher I_D/I_G ratios, respectively (table 3.5) in P-CNT and N-CNT, are attributed to CNT surface coverage (thereby more defects coverage) by PDDA polymer in the former[53,54], and the Nafion® chain radical functionalization in the latter.[45,46] The N 1s XPS spectra show its dominant presence in P-CNT compared to unmodified CNT and N-CNT due to the presence of quaternary ammonium groups in the former further shows the functionalization (Figure 3.5d).

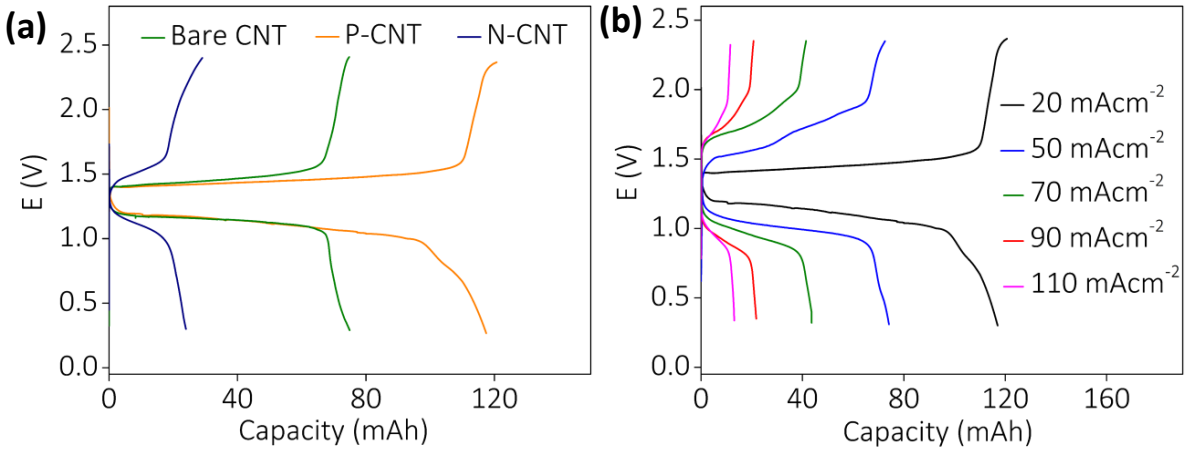

Figure: 3.13. (a) Charge-discharge curves for with unmodified CNT, P-CNT & N-CNT electrodes at 20 mA/cm^2 in battery configuration. **(b)** Rate capability plot with P-CNT electrode.

The discharge curves of the battery with P-CNT, N-CNT, and unmodified CNT are shown in figure 3.13a. The discharge capacities are noticeably increased with P-CNT compared to unmodified CNT; however, it was very inferior with the N-CNT electrode validating the fact that the battery performance with negatively charged electroactive redox species can be targeted by activating Coulombic forces. The higher battery performance with P-CNT compared to N-CNT is mainly due to gated

molecular flux at the interface resulting in an electrostatic current contribution parallel to diffusion current, which in turn can extend the concentration polarization region (figure 3.13a, 3.13b). The pre-concentration of the redox species at the P-CNT/electrolyte interface as noted earlier can further lead to enhanced charge transfer. It is clear that the time of discharge is extended noticeably due to the Coulombic attraction of electroactive redox species by the driving P-CNT electrode (figure 3.13a). These results and previous investigations taken together, the higher performance of battery with the P-CNT electrode is primarily due to Coulombic force gated molecular flux within the reaction that triggers an electrostatic current contribution parallel to the diffusion.

CHAPTER 4

CONCLUSION

The physical processes of molecular transport play a central role in the electrochemical behavior of reversible redox species as their extremely faster electron transfer event demands the reacting species to reach the interface most often by simple diffusion. Even under convective fluid flow as the thickness of the hydrodynamic boundary layer or Prandtl layer is ~10 times larger than the diffusion layer, simple diffusion predominates the transport phenomena within the reaction zone. Therefore, these ubiquitous physical phenomena pose unique challenges to utilize the full potential of reversible redox molecules either by the electrode or fluid characteristics. This study shows that by activating Coulombic forces at the electrochemical interface, molecular transport can be directed towards the electrode with an electrostatic current contribution parallel to the diffusion current. We show that Coulombic force gated molecular flux can almost double the volumetric energy density of iron flow batteries by extending the battery performance well beyond the conventional concentration polarization regime.

REFERENCES

1. Armstrong, R. C.; Wolfram, C.; Jong, K. P.; Gross, R.; Lewis, N. S.; Boardman, B.; Ragauskas, A. J.; Martinez, K. E.; Crabtree, G.; Ramana, M. V. The frontiers of energy, *Nat. Energy*, **2016**, *1*.
2. Scrosati, B.; Hassoun,J.; Sun, Y. Lithium-ion batteries. A look into the future, *Energy Environ. Sci.*, **2011**, *4*, 3287-3295.
3. Goeppert, A.; Czaun, M.; Prakash, G. K. S.; Olah, G. A. Air as the renewable carbon source of the future: an overview of CO_2 capture from the atmosphere, *Energy Environ. Sci.*, **2012**, *5*, 7833-7853.
4. Mourad, E.; Coustan, L.; Lannelongue, P.; Zigah, D.; Mehdi, A.; Vioux, A.; Freunberger, S. A.; Favier, F.; Fontaine, O. Biredox Ionic Liquids with Solid-like Redox Density in the Liquid State for High-Energy Supercapacitors. *Nat. Mater.* **2016**, *16*, 446-453.
5. Choi, N.-S.; Chen, Z.; Freunberger, S. A.; Ji, X.; Sun, Y.-K.; Amine, K.; Yushin, G.; Nazar, L. F.; Cho, J.; Bruce, P. G. Challenges Facing Lithium Batteries and Electrical Double-Layer Capacitors. *Angew. Chem. Int. Ed.* **2012**, *51* (40), 9994–10024.
6. Winter, M; Brodd, R. J. What are Batteries, Fuel Cells, and Supercapacitors? *Chem. Rev.* **2004**, *104* (10), 4245-4269.
7. Chinnam, P. R.; Fall, B.; Dikin, D. A.; Jalil, A.; Hamilton, C. R.; Wunder, S. L.; Zdilla, M. J. A Self-Binding, Melt-Castable, Crystalline Organic Electrolyte for Sodium Ion Conduction. *Angew. Chem. Int. Ed.* **2016**, *128* (49), 15480–15483.
8. Tarascon, J.-M.; Armand, M. Issues and Challenges Facing Rechargeable Lithium Batteries. *Nature* **2001**, *414*, 359.
9. Chen, J.-J.; Ye, J.-C.; Zhang, X.-G.; Symes, M. D.; Fan, S.-C.; Long, D.-L.; Zheng, M.-S.; Wu, D.-Y.; Cronin, L.; Dong, Q.-F. Design and Performance of Rechargeable Sodium Ion Batteries, and Symmetrical Li-Ion Batteries with Supercapacitor-Like Power Density Based upon Polyoxovanadates. *Adv. Energy Mater.* **2018**, *8* (6), 1701021.

10. Li, B.; Nie, Z.; Vijayakumar, M.; Li, G.; Liu, J.; Sprenkle, V.; Wang, W. Ambipolar Zinc-Polyiodide Electrolyte for a High-Energy Density Aqueous Redox Flow Battery. *Nat Commun.* **2015**, *6*, 6303.
11. Sathiya, M.; Prakash, S. A.; Ramesha, K.; Shukla, K. A. Nitrate-Melt Synthesized HT-LiCoO2 as a Superior Cathode-Material for Lithium-Ion Batteries. *Materials* **2009**, *2*, 857-868.
12. Miroshnikov, M.; Divya, K. P.; Babu, G.; Meiyazhagan, A.; Reddy Arava, L. M.; Ajayan, P. M.; John, G. Power from Nature: Designing Green Battery Materials from Electroactive Quinone Derivatives and Organic Polymers. *J. Mater. Chem. A* **2016**, *4* (32), 12370–12386.
13. Singh, D. K.; Krishna, K. S.; Harish, S.; Sampath, S.; Eswaramoorthy, M. No More HF: Teflon-Assisted Ultrafast Removal of Silica to Generate High-Surface-Area Mesostructured Carbon for Enhanced CO_2 Capture and Supercapacitor Performance. *Angew. Chem. Int. Ed.* **2016**, *55* (6), 2032–2036.
14. Gong, K.; Xu, F.; Grunewald, J. B.; Ma, X.; Zhao, Y.; Gu, S.; Yan, Y. All-Soluble All-Iron Aqueous Redox-Flow Battery. *ACS Energy Letters,* **2016**, *1*(1), 89–93. DOI:10.1021/acsenergylett.6b00049
15. Lu, Y.; Goodenough, J. B.; Kim, Y. Aqueous Cathode for Next-Generation Alkali-Ion Batteries. *J. Am. Chem. Soc.* **2011**, *133* (15), 5756–5759.
16. Yuan, Z.; Duan, Y.; Liu, T.; Zhang, H.; Li, X. Toward a Low-Cost Alkaline Zinc-Iron Flow Battery with a Polybenzimidazole Custom Membrane for Stationary Energy Storage. *iScience* **2018**, *3*, 40–49.
17. Selverston, S.; Savinell, R. F.; Wainright, J. S. Zinc-Iron Flow Batteries with Common Electrolyte. *J. Electrochem. Soc.* **2017**, *164* (6), 1069–1075.
18. Esswein, A. J.; Goeltz, J.; Amadeo, D. High solubility iron hexacyanides, *U. S. Patent App. US20140051003* A1, **2014**, *1*.
19. Gong, K.; Ma, X.; Conforti, K. M.; Kuttler, K. J.; Grunewald, J. B.; Yeager, K. L.; Bazant, M. Z.; Gu, S.; Yan, Y. A Zinc–iron Redox-Flow Battery under $100 per KW h of System Capital Cost. *Energy Environ. Sci.* **2015**, *8* (10), 2941–2945.
20. Bhat, Z. M.; Thimmappa, R.; Devendrachari, M. C.; Shafi, S. P.; Aralekallu, S.; Kottaichamy, A. R.; Gautam, M.; Thotiyl, M. O. A Direct Alcohol Fuel Cell Driven by an Outer Sphere Positive Electrode. *J. Phys. Chem. Lett.* **2017**, *8* (15), 3523–3529.

21. Luo, J.; Hu, B.; Debruler, C.; Bi, Y.; Zhao, Y.; Yuan, B.; Hu, M.; Wu, W.; Liu, T. L. Unprecedented Capacity and Stability of Ammonium Ferrocyanide Catholyte in PH Neutral Aqueous Redox Flow Batteries. *Joule* **2019**, *3* (1), 149–163.
22. Orita, A.; Verde, M. G.; Sakai, M.; Meng, Y. S. A Biomimetic Redox Flow Battery Based on Flavin Mononucleotide. *Nat Commun.* **2016**, *7*, 13230.
23. Luo, J.; Sam, A.; Hu, B.; DeBruler, C.; Wei, X.; Wang, W.; Liu, T. L. Unraveling PH Dependent Cycling Stability of Ferricyanide/Ferrocyanide in Redox Flow Batteries. *Nano Energy* **2017**, *42*, 215–221.
24. Winsberg, J.; Hagemann, T.; Janoschka, T.; Hager, M. D.; Schubert, U. S. Redox-Flow Batteries: From Metals to Organic Redox-Active Materials. *Angew. Chem. Int. Ed.* **2017**, *56* (3), 686–711.
25. Wedege, K.; Azevedo, J.; Khataee, A.; Bentien, A.; Mendes, A. Direct Solar Charging of an Organic–Inorganic, Stable, and Aqueous Alkaline Redox Flow Battery with a Hematite Photoanode. *Angew. Chem. Int. Ed.* **2016**, *55* (25), 7142–7147.
26. Ji, X.; Banks, C. E.; Crossley, A.; Compton, R. G. Oxygenated Edge Plane Sites Slow the Electron Transfer of the Ferro-/Ferricyanide Redox Couple at Graphite Electrodes. *ChemPhysChem* **2006**, *7* (6), 1337–1344.
27. Nugent, J. M.; Santhanam, K. S. V; Rubio, A.; Ajayan, P. M. Fast Electron Transfer Kinetics on Multiwalled Carbon Nanotube Microbundle Electrodes. *Nano Lett.* **2001**, *1* (2), 87–91.
28. Curtis, J. C.; Meyer, T. J. Outer-Sphere Charge Transfer in Mixed-Metal Ion Pairs. *Inorg. Chem.* **1982**, *21* (4), 1562–1571.
29. Velický, M.; Bradley, D. F.; Cooper, A. J.; Hill, E. W.; Kinloch, I. A.; Mishchenko, A.; Novoselov, K. S.; Patten, H. V; Toth, P. S.; Valota, A. T.; et al. Electron Transfer Kinetics on Mono- and Multilayer Graphene. *ACS Nano* **2014**, *8* (10), 10089–10100.
30. Shevchuk, I. V. Turbulent Heat and Mass Transfer over a Rotating Disk for the Prandtl or Schmidt Numbers Much Larger than Unity: An Integral Method. *Heat and Mass Transfer* **2009**, *45* (10), 1313–1321.
31. Wang, J. *Analytical Electrochemistry, Third Edition* **2006**. DOI:10.1002/0471790303.

32. Kim, S.; Vijayakumar, M.; Wang, W.; Zhang, J.; Chen, B.; Nie, Z.; Chen, F.; Hu, J.; Li, L.; Yang, Z. Chloride Supporting Electrolytes for All-Vanadium Redox Flow Batteries. *Phys. Chem. Chem. Phys.* **2011**, *13* (40), 18186–18193.
33. Chen, Y.; Zhou, M.; Xia, Y.; Wang, X.; Liu, Y.; Yao, Y.; Zhang, H.; Li, Y.; Lu, S.; Qin, W.; et al. A Stable and High-Capacity Redox Targeting-Based Electrolyte for Aqueous Flow Batteries. *Joule* **2019**. DOI: 10.1016/j.joule.2019.06.007
34. Elgrishi, N.; Routree, K. J.; McCarthy, B. D.; Routree, E. S.; Eisenhart, T. T.; Dempsy, J. L. A Practical Beginnner's Guide to Cyclic Voltammetry. *J. Chem. Educ.* **2018**, *95,* 197-206.
35. Fragkou, V;, Ge, Y.; Steiner, G.; Freeman, D.; Bartetzko, N.; Turner, A. P. F. Determination of the real surface area of a screen-printed electrode by chronocoulometry. *Int. J. Electro. Sci.*, **2012**, *7*(7), 6214-6220.
36. Hosseini, S.; Lao-atiman, W.; Han, S. J.; Arpornwichanop, A.; Yonezawa, T.; Kheawhom, S. Discharge Performance of Zinc-Air Flow Batteries Under the Effects of Sodium Dodecyl Sulfate and Pluronic F-127. *Sci Rep.* **2018**, *8* (1), 14909.
37. Wan, F.; Zhang, L.; Dai, X.; Wang, X.; Niu, Z.; Chen, J. Aqueous Rechargeable Zinc/Sodium Vanadate Batteries with Enhanced Performance from Simultaneous Insertion of Dual Carriers. *Nat Commun.* **2018**, *9* (1), 1656.
38. Mooste, M.; Kibena-Põldsepp, E.; Marandi, M.; Matisen, L.; Sammelselg, V.; Tammeveski, K. Electrochemical Properties of Gold and Glassy Carbon Electrodes Electrografted with an Anthraquinone Diazonium Compound Using the Rotating Disc Electrode Method. *RSC Adv.* **2016**, *6* (47), 40982–40990.
39. Tucceri, R. The Charge Transport Process at Gold Electrodes Modified by Thick Nickel Hydroxide Films. A Study Employing Rotating Disc Electrode Voltammetry in the Presence of the $Fe(CN)_6^{3-/4-}$ Redox Couple. *J. Electroanal. Chem.* **2016**, *782*, 125–132.
40. Zhang, X.; Chen, M.; Yu, Y.; Yang, T.; Wang, J. Polyelectrolyte-Modified Multi-Walled Carbon Nanotubes for the Adsorption of Chromium(VI). *Anal. Methods* **2011**, *3* (2), 457–462.
41. Kaur, P.; Shin, M.-S.; Joshi, A.; Kaur, N.; Sharma, N.; Park, J.-S.; Sekhon, S. S. Interactions between Multiwall Carbon Nanotubes and Poly(Diallyl Dimethylammonium) Chloride: Effect of the Presence of a Surfactant. *J. Phys. Chem. B* **2013**, *117* (11), 3161–3166.

42. Du, Z.; Yu, Y.-L.; Wang, J.-H. Functionalization of Multi-Walled Carbon Nanotubes and Their Application for Selective Isolation of Acidic Proteins. *Macromol. Biosci.* **2009**, *9* (1), 55–62.
43. Wang, S.; Yu, D.; Dai, L. Polyelectrolyte Functionalized Carbon Nanotubes as Efficient Metal-Free Electrocatalysts for Oxygen Reduction. *J. Am. Chem. Soc.* **2011**, *133* (14), 5182–5185.
44. Liu, Y. L.; Su, Y. H.; Chang, C. M.; Suryani, Wang, D. M.; Lai, J.-Y. Preparation and applications of Nafion-functionalized multiwalled carbon nanotubes for proton exchange membrane fuel cells. *J. Mat. Chem.* **2010***, 20(21),* 4409*.* DOI:10.1039/c000099j
45. Rambabu, G.; Nagaraju, N.; Bhat, S. D.; Functionalized fullerene embedded in Nafion matrix: A modified composite membrane electrolyte for direct methanol fuel cells. *Chem. Eng. J.* **2016***, 306*, 43–52*.* DOI: 10.1016/j.cej.2016.07.032
46. Sarkar, A.; Chakraborty, A. K.; Bera, S.; Krishnamurthy, S. Novel Hydrothermal Synthesis of CoS2/MWCNT Nanohybrid Electrode for Supercapacitor: A Systematic Investigation on the Influence of MWCNT. *J. Phys. Chem. C* **2018**, *122* (32), 18237–18246.
47. Li, J.; Feng, H.; Jiang, J.; Feng, Y.; Xu, Z.; Qian, D. One-Pot in Situ Synthesis of a CoFe2O4 Nanoparticle-Reduced Graphene Oxide Nanocomposite with High Performance for Levodopa Sensing. *RSC Adv.* **2015**, *5* (121), 99669–99677.
48. Mohammadi, N.; Adeh, N. B.; Najafi, M. A Highly Defective Mesoporous Carbon – Ionic Liquid Paste Electrode toward the Sensitive Electrochemical Determination of Rutin. *Anal. Methods* **2017**, *9* (1), 84–93.
49. Xiao, P.; Cai, Y.; Chen, X.; Sheng, Z.; Chang, C. Improved Electrochemical Performance of LiFe0.4Mn0.6PO4/C with Cr3+ Doping. *RSC Adv.* **2017**, *7* (50), 31558–31566.
50. Guo, H.; Zhang, X.; He, W.; Yang, X.; Liu, Q.; Li, M.; Wang, J. Fabricating Three-Dimensional Mesoporous Carbon Network-Coated LiFePO4/Fe Nanospheres Using Thermal Conversion of Alginate-Biomass. *RSC Adv.* **2016**, *6* (21), 16933–16940.
51. Wang, S.; Zhao, X.; Cochell, T.; Manthiram, A. Nitrogen-Doped Carbon Nanotube/Graphite Felts as Advanced Electrode Materials for Vanadium Redox Flow Batteries. *J. Phys. Chem. Lett.* **2012**, *3* (16), 2164–2167.

52. Ek-Weis, J.; Costa, S.; Frank, O.; Kalbac, M. Heating Isotopically Labeled Bernal Stacked Graphene: A Raman Spectroscopy Study. *J. Phys. Chem. Lett.* **2014**, *5* (3), 549–554.
53. Wang, D.; Lu, S.; Kulesza, P. J.; Li, C. M.; De Marco, R.; Jiang, S. P. Enhanced Oxygen Reduction at Pd Catalytic Nanoparticles Dispersed onto Heteropolytungstate-Assembled Poly(Diallyldimethylammonium)-Functionalized Carbonnanotubes. *Phys. Chem. Chem. Phys.* **2011**, *13* (10), 4400–4410.
54. Wang, S.; Jiang, S. P.; Wang, X. Polyelectrolyte Functionalized Carbon Nanotubes as a Support for Noble Metal Electrocatalysts and Their Activity for Methanol Oxidation. *Nanotechnology* **2008**, *19* (26), 265601.
55. Fadel, M.; Daurelle, J.-V.; Fourmond, V.; Vicente, J. A New Electrochemical Cell with a Uniformly Accessible Electrode to Study Fast Catalytic Reactions. *Phys. Chem. Chem. Phys.* **2019**, *21* (23), 12360–12371.
56. Kear, G.; Barker, B. D.; Stokes, K.; Walsh, F. C. Flow Influenced Electrochemical Corrosion of Nickel Aluminium Bronze – Part I. Cathodic Polarisation. *J. Appl. Electrochem.* **2004**, *34* (12), 1235–1240.